processes

Article

Applications of Differential Effective Medium (DEM)-Driven Correlations to Estimate Elastic Properties of Jafurah Tuwaiq Mountain Formation (TMF)

Ali Shawaf, Vamegh Rasouli * and Abdesselem Dehdouh

Energy and Petroleum Engineering Department, University of Wyoming, Laramie, WY 82071, USA; aalshawa@uwyo.edu (A.S.); adehdouh@uwyo.edu (A.D.)
* Correspondence: vrasouli@uwyo.edu

Abstract: Organic-rich mud rocks are being developed on a large scale worldwide, including in the Middle East. The Jurassic Tuwaiq Mountain Formation (TMF) in the Jafurah Basin is a potential world-class unconventional play. Based on a petrophysical evaluation of the Jafurah basin, the TMF exhibits exceptional and unconventional gas characteristics, such as a high total organic content (TOC) and low clay content. Additionally, the TMF is in the appropriate maturity window, indicating that it has reached the required level of thermal maturity to generate hydrocarbons. Plans for the development of the Jafurah unconventional field use multistage hydraulic fracturing technology. The elastic properties of the shale formation, particularly its Young's modulus and Poisson's ratio, dictate how the rock responds to stress and deformation. These properties strongly impact the growth of hydraulic fractures in shale formations. Without a comprehensive understanding of the elastic properties, predicting the bulk mechanical response of the target zones and surrounding layers would be challenging. Therefore, this study aims to predict the elastic characteristics of the Jafurah shale play considering the variations in carbonate facies, the kerogen volume fraction, and the pore's geometry. Petrophysical and XRD data were used to estimate the elastic properties of various tiers (geological units) of the TMF (Tiers 1, 2, and 3). Inclusion-based, differential effective medium (DEM) rock physics models were used to estimate the formation's elastic and velocity properties as a function of the kerogen volume fraction and the pore's geometry. The results showed that the Young's modulus as well as the mineral and elastic brittleness indices increase as the volume fraction of calcite increases. At the same time, they decrease due to intensified clay and kerogen volumes. The effect of the TMF's elastic parameters on the rock brittleness behavior was also investigated by considering the formation's mineralogy, as well as clay and kerogen contents. The results led to the development of physics-based correlations of the mineral brittleness index as function of the Young's modulus and Poisson's ratio for various tiers of the TMF.

Keywords: Jafurah; Eagle Ford; elastic properties; stiffness; brittleness index

Citation: Shawaf, A.; Rasouli, V.; Dehdouh, A. Applications of Differential Effective Medium (DEM)-Driven Correlations to Estimate Elastic Properties of Jafurah Tuwaiq Mountain Formation (TMF). *Processes* **2023**, *11*, 1643. https://doi.org/10.3390/pr11061643

Academic Editor: Qingbang Meng

Received: 24 April 2023
Revised: 22 May 2023
Accepted: 26 May 2023
Published: 27 May 2023

1. Introduction

Increasing worldwide energy demands and the depletion of traditional hydrocarbon reservoirs have driven the industry to expedite the exploration of unconventional resources. Resources refer to oil and gas geological formations characterized by having a low porosity, ultra-low reservoir permeability, poor pore-scale connectivity, and high total organic content [1,2]. The permeability of unconventional formations is usually less than 0.1 mD (in the range of micro- to nano-Darcy), and hydraulic fracturing (HF) stimulations are required to economically produce hydrocarbons from these resources [3]. Examples of unconventional resources include shale gas, shale oil, tight sands, coal bed methane, heavy oil, and gas hydrates [4,5].

An accurate estimation of the elastic properties of shale plays is essential for the design of hydraulic fracturing and fracture spacing determination [6] and is the leading research objective of this project. Different inclusion-based rock physics models have been developed to estimate the elastic properties of other formations as a function of porosity, pore fluid types, saturation, and pore geometry. These models are summarized in [7,8]. Among these models, effective differential medium (DEM) has shown advantages by considering the order of adding inclusions into the composition and the effect of different inclusion sizes.

Harju 2023 [8] investigated the effect of mineral composition on the elastic properties of sedimentary rocks using laboratory measurements and computational modeling. Their study focused on various different sedimentary rocks from the Bakken shale formation with varying mineral compositions, including sandstones, siltstones, and shales. The results showed that mineral composition has a significant impact on the elastic properties of sedimentary rocks. Specifically, the presence of clay minerals in shales and siltstones was found to decrease the elastic properties, such as the Young's modulus and Poisson's ratio, while the presence of quartz in sandstones increased these properties [9]. The authors of [10] developed rock physics correlations to estimate the elastic properties of the Bakken formation based on Harju's work. Their study used well log data and rock core samples to derive empirical relationships between elastic properties, such as the Young's modulus, Poisson's ratio, and bulk modulus, and other geophysical parameters, such as density, sonic velocity, and resistivity. The results showed that the developed rock physics correlations had a high degree of accuracy in predicting the elastic properties of the Bakken formation. The study also demonstrated the importance of incorporating the mineralogy and pore geometry of the shale reservoir into rock physics models to account for the complex nature of the Bakken formation. Recently [11] applied a modified DEM model to estimate the elastic properties of the Duvernay shale formation. Their study showed that the modified DEM model, which incorporated the effects of pore size distribution and clay content, could accurately predict the elastic properties of the shale formation based on well log data. The study also demonstrated that the modified DEM model could be used to estimate the changes in elastic properties due to changes in pore pressure and effective stress. These recent studies reveal the potential of DEM models to accurately assess the elastic properties of shale formations, which can have important implications for optimizing hydraulic fracturing designs and improving shale reservoir characterization.

The goal of this study was to predict the elastic behavior of the Jafurah shale play considering the variations in carbonate facies, the kerogen volume fraction, and the pore's geometry. An accurate estimation and employment of the elastic moduli is essential to optimize the design of hydraulic fracturing treatments and maximize hydrocarbon recovery. Available petrophysical and XRD data were used to estimate the elastic properties of various tiers (geological units) of the TMF (Tier 1, 2, and 3). Inclusion-based, differential effective medium (DEM) rock physics models were used to estimate the formation's elastic and velocity properties as a function of the kerogen volume fraction and the pore's geometry (aspect ratio, AR). DEM-base correlations were applied to estimate the compressional and shear velocities as well as the elastic parameters of the TMF, assuming different pore aspect ratios. The results of which were compared with the Eagle Ford Shale in North America, as an analogue to the TMF. The findings of this study have important implications for various applications in the oil and gas industries, including hydraulic fracturing and reservoir characterization.

2. DEM-Based Correlations

The differential effective medium (DEM) theory, proposed by [12], is utilized for modeling two-phase composites. This method involves the progressive addition of inclusions to the matrix phase. It is employed to determine the effective elastic properties of porous rocks that are either dry or saturated with fluids.

Consider a two-phase composite comprising a matrix phase (phase 1) with a volume fraction x_1 and an included phase (phase 2) with a volume fraction x_2. Assuming the effective bulk and shear moduli $K^*(x_2)$ and $\mu^*(x_2)$ at one value of x_2 are known, $K^*(x_2)$ and

$\mu^*(x_2)$ can be treated as the composite host bulk and shear moduli. Then, $K^*(x_2 + \Delta\, x_2)$ and $\mu^*(x_2 + \Delta\, x_2)$ represent the effective bulk and shear moduli when a small fraction of the composite host $(\Delta\, x_2/(1 - x_2))$ is replaced by inclusions of phase 2. To numerically solve for the bulk and shear moduli of the effective medium, the following equations are utilized:

$$(1 - x_2)\frac{dK^*(x_2)}{dx_2} = (K_2 - K^*)P^{*2}(x_2) \tag{1}$$

$$(1 - x_2)\frac{d\mu^*(x_2)}{dx_2} = (\mu_2 - \mu^*)Q^{*2}(x_2) \tag{2}$$

For the initial conditions, $K^*(0) = K_1$, $\mu^*(0) = \mu_1$, K_1 and μ_1 are the bulk and shear moduli of the initial host material, and K_2 and μ_2 are the bulk and shear moduli of the incrementally added inclusions, respectively.

Bing and Jia 2014 [13] summarised the DEM features for modeling the effective elastic medium of rocks as follows:

- Compared with other methods such as the Kuster–Toksöz theory, it can never violate rigorous bounds;
- Developing numerical solutions of differential equations is needed to accurately estimate the bulk and shear moduli;
- The order of different inclusions (i.e., pores or cracks) with varying aspect ratios significantly impacts the effective elasticities of the porous medium.

The pore's aspect ratio (AR) is the ratio between the smallest and largest diameter of the pore. Pores with an AR of 1 have a spherical shape, while those with an AR close to 0 have a crack-like shape. Types of pore geometries can be characterized by typical values of AR, such as 0.01 for crack-type pores, 0.05 for intergranular pores, 0.15 for interparticle pores, and 0.80 for moldic pore geometries [10]. Figure 1 shows examples of moldic, inter-particle (inter-crystal), and fracture pore types [14]. As the aspect ratio increases, the pores become stiffer, and therefore, the velocity increases.

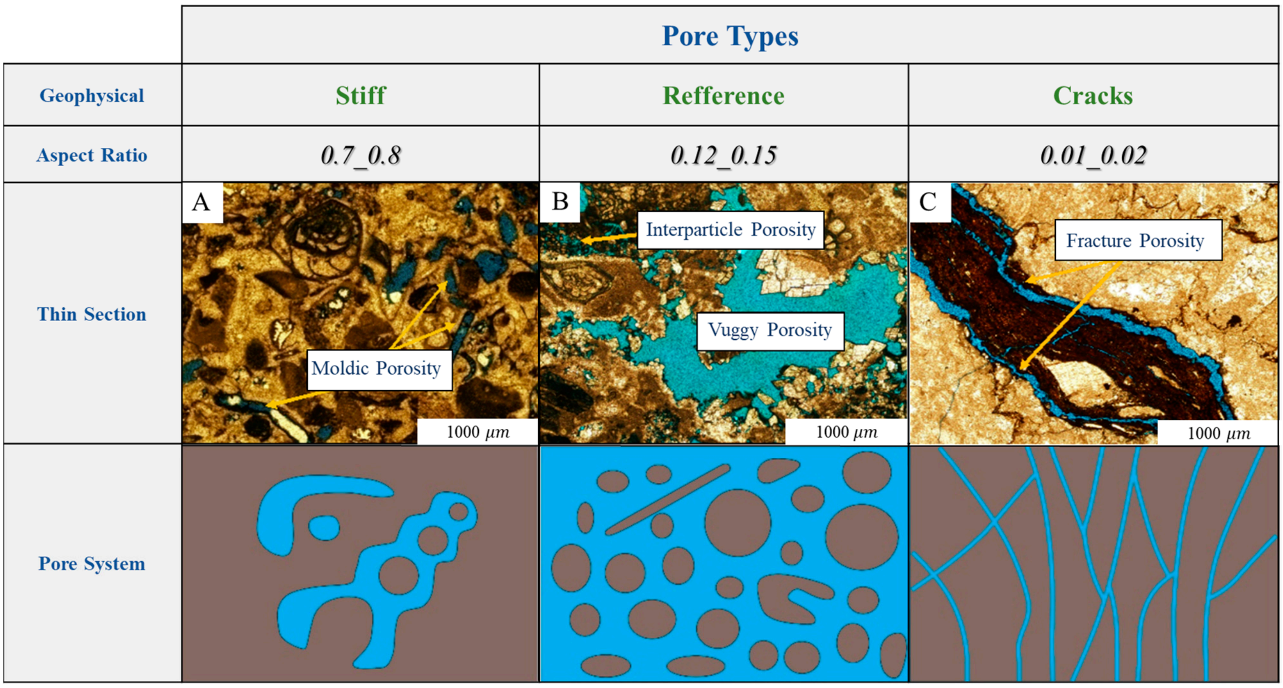

Figure 1. Examples of moldic (**A**), inter-particle (**B**), and fracture (**C**) pore types [15].

In inclusion-based models, it is common to use the Brie model to mix the fluid phases. The author of [16] proposed the following empirical fluid-mixing law:

$$K_{\text{fluid mix}} = \left(K_{\text{liquid}} - K_{\text{gas}}\right)\left(1 - S_{\text{gas}}\right)^{e} + K_{\text{gas}} \tag{3}$$

$$K_{\text{liquid}} = \frac{\left(S_{\text{water}} + S_{\text{oil}}\right)}{S_{\text{water}}/K_{\text{water}} + S_{\text{oil}}/K_{\text{oil}}} \tag{4}$$

The simple Reuss rock physics model is derived when the mixing coefficient (e) is assigned a value of −1, corresponding to a weak formation and equivalent to a homogeneous saturation. On the other hand, when e = 1, it converges to the Voigt rock physics model, representing a solid rock and equivalent to inhomogeneous saturation. Field data suggest an average value of e between 3 and 5. Despite its capabilities, using the DEM model requires solving differential equations, which is not straightforward and cannot be easily developed.

Extensive correlations were developed by [9] through numerous discrete element method (DEM) simulations. These correlations aimed to establish a relationship between a single-phase rock's compressional and shear velocities considering various saturations (water, oil, gas) and pore aspect ratios (AR). A coefficient of e = 3 accounted for the fluid mixing for all the correlations. The properties of minerals corresponding to the Bakken formation were utilized in this study. Table 1 [8] shows the bulk (K) and shear (μ) moduli and density (ρ) of minerals, and Table 2 [8] shows the properties of the water, oil, and gas used for developing the correlations.

Table 1. Bulk moduli (K), shear moduli (μ), density (ρ), and compressional (V_p) and shear (V_s) velocities of minerals used in this study for modeling.

Minerals	Calcite	Chlorite	Dolomite	Pyrite	Cristobalite	Illite	Quartz	Smectite
K (MPa)	76.8	95.3	94.7	158	39.1	11.7	36.6	9.3
μ (MPa)	32.0	11.4	45.0	149	16.3	16.4	45.0	6.9
ρ (gr/cc)	2.71	2.69	2.87	5.02	2.32	2.60	2.65	2.20
Vp (Km/s)	6.64	6.41	7.34	8.43	5.12	3.59	6.04	2.90
Vs (Km/s)	3.44	2.06	3.96	5.45	2.65	2.51	4.12	1.77

Table 2. Bulk moduli (K), density (ρ), and equivalent velocity (V_p) of pore fluids.

Fluid	Oil	Water	Gas
K (MPa)	0.42	2.2	0.15
ρ (gr/cc)	0.8	1.1	0.015
V_p (Km/s)	0.725	1.414	3.162

The elastic bulk (K) and shear (μ) moduli can be converted to the compressional (V_p) and shear (V_s) velocities using the following isotropic equations [17]:

$$V_P = \sqrt{\frac{K + 4/3\mu}{\rho}},\ V_S = \sqrt{\frac{\mu}{\rho}} \tag{5}$$

For the compressional velocity (V_p), the correlations are divided based on the range of the pore's aspect ratio as being less than 0.1 or equal or greater than 0.1. For the shear velocity (V_s), the same correlations are used regardless of the value of the pore's aspect ratio.

The Helm's correlations are presented as follows:

Case 1: Compressional Velocity (V_p), AR < 0.1

$$V_p = \left(V_{p,m} - C_o\right)e^{-C_1\phi} + C_o \tag{6}$$

$$C_0 = \mathrm{A}.AR^2 + \mathrm{B}.AR + \mathrm{C} \tag{7}$$

$$C_1 = \mathrm{A}.AR^{\mathrm{B}} \tag{8}$$

Case 2: Compressional Velocity (V_{p}), AR ≥ 0.1

$$V_p = V_{p,m}e^{-C_o\phi} \tag{9}$$

$$C_0 = \mathrm{A}.AR^{\mathrm{B}} \tag{10}$$

Case 3: Shear Velocity (V_{s}), AR < 0.1 and AR ≥ 0.1

$$V_s = V_{s,m}e^{-C_1'\phi} \tag{11}$$

$$C_1' = \mathrm{A}.AR^{\mathrm{B}} \tag{12}$$

where:

$$\begin{array}{c} \mathrm{A} = \mathrm{a}_0 S_{\mathrm{o}}^2 + \mathrm{a}_1 S_{\mathrm{o}} + \mathrm{a}_2 \;\; \mathrm{B} = \mathrm{m}_0 S_{\mathrm{o}}^2 + \mathrm{m}_1 S_{\mathrm{o}} + \mathrm{m}_2,\; \mathrm{C} = \mathrm{m}_0 S_{\mathrm{o}}^2 + \mathrm{m}_1 S_{\mathrm{o}} + \mathrm{m}_2 \\ \mathrm{a}_0 = \mathrm{p}_1 S_{\mathrm{w}}^2 + \mathrm{p}_2 S_{\mathrm{w}} + \mathrm{p}_3 \; \mathrm{m}_0 = \mathrm{q}_1 S_{\mathrm{w}}^2 + \mathrm{q}_2 S_{\mathrm{w}} + \mathrm{q}_3 \;\; \mathrm{n}_0 = \mathrm{r}_1 S_{\mathrm{w}}^2 + \mathrm{r}_2 S_{\mathrm{w}} + \mathrm{r}_3 \\ \mathrm{a}_1 = \mathrm{p}_4 S_{\mathrm{w}}^2 + \mathrm{p}_5 S_{\mathrm{w}} + \mathrm{p}_6 \; \mathrm{m}_1 = \mathrm{q}_4 S_{\mathrm{w}}^2 + \mathrm{q}_5 S_{\mathrm{w}} + \mathrm{q}_6 \; \mathrm{n}_0 = \mathrm{r}_4 S_{\mathrm{w}}^2 + \mathrm{r}_5 S_{\mathrm{w}} + \mathrm{r}_6 \\ \mathrm{a}_2 = \mathrm{p}_7 S_{\mathrm{w}}^2 + \mathrm{p}_8 S_{\mathrm{w}} + \mathrm{p}_9 \;\; \mathrm{m}_2 = \mathrm{q}_7 S_{\mathrm{w}}^2 + \mathrm{q}_8 S_{\mathrm{w}} + \mathrm{q}_9 \;\; \mathrm{n}_0 = \mathrm{r}_7 S_{\mathrm{w}}^2 + \mathrm{r}_8 S_{\mathrm{w}} + \mathrm{r}_9 \end{array} \tag{13}$$

Table 3 presents all the constants of the above correlations for calcite, as an example. The constants for other minerals can be found in [9].

Table 3. Using DEM-based developed correlations, constants p, q, and r for calcite were used to estimate velocities as a function of fluid saturations and pore's aspect ratio.

$V_{\mathrm{p}}, AR < 0.1,\ V_p = (V_{p,m} - C_o)e^{-C_1\phi} + C_o,\ C_0 = \mathrm{A}.\mathrm{AR}^2 + \mathrm{B}.AR + \mathrm{C},\ C_1 = \mathrm{A}.AR^{\mathrm{B}}$								
p1	**p2**	**p3**	**p4**	**p5**	**p6**	**p7**	**p8**	**p9**
1261.601	−549.347	122.612	−266.118	313.338	−93.760	189.694	−115.373	−67.684
q1	q2	q3	q4	q5	q6	q7	q8	q9
−115.601	38.394	−7.773	9.075	−12.784	5.612	−18.841	10.237	3.741
r1	r2	r3	r4	r5	r6	r7	r8	r9
3.421	−2.120	0.978	−3.084	3.737	−0.450	1.307	−0.134	0.566
$V_{\mathrm{p}}, AR \geq 0.1,\ V_p = V_{p,m}e^{-C_o\Phi},\ C_0 = \mathrm{A}.AR^{\mathrm{B}}$								
p1	p2	p3	p4	p5	p6	p7	p8	p9
−0.0641	−0.0227	−0.0256	−0.0598	−0.0249	0.1104	−0.0978	0.3036	0.6622
q1	q2	q3	q4	q5	q6	q7	q8	q9
0.0269	0.0146	0.0394	−0.0158	0.0748	0.0370	0.0631	0.1127	−0.5686
$Vs, AR < 0.1,\ V_s = V_{s,m}e^{-C_1'\Phi},\ C_1' = \mathrm{A}.AR^{\mathrm{B}}$								
p1	p2	p3	p4	p5	p6	p7	p8	p9
0.054	−0.012	−0.104	0.159	−0.318	0.066	−0.178	0.103	0.435
q1	q2	q3	q4	q5	q6	q7	q8	q9
0.125	−0.114	−0.028	−0.102	−0.008	0.038	−0.082	0.083	−0.747
$Vs, AR \geq 0.1,\ V_s = V_{s,m}e^{-C_1'\Phi},\ C_1' = \mathrm{A}.AR^{\mathrm{B}}$								
p1	p2	p3	p4	p5	p6	p7	p8	p9
11.009	−4.952	0.141	−5.585	2.514	0.029	−0.030	0.301	0.460
q1	q2	q3	q4	q5	q6	q7	q8	q9
12.810	−5.748	0.027	−6.344	2.886	−0.019	−0.010	0.209	−0.582

In this study, we use the above correlations to estimate the velocity and elastic properties of the TMF formation based on the XRD data. A comparison of our results with those of the limited published data will support the reliability of the hydraulic fracturing spacing models.

3. Area of Study and Characteristics of TMF

The Jafurah liquid-rich shale play is located east of the greater Ghawar field, which is the world's largest conventional oil field located in the eastern region of Saudi Arabia (see Figure 2) [18,19]. Based on exploration and appraisal programs, the ultimate recovery of the natural gas and liquids from the play is estimated to be around 200 trillion cubic feet equivalent (tcfe), and the first commercial production is scheduled to start in 2025 [20,21]. Based on a petrophysical evaluation of the Jafurah basin, our primary target formation is the Jurassic Tuwaiq Mountain (TMF) formation, which is the principal source rock of the prolific Arab-D carbonate reservoir, as shown in Figure 3 [20,21]. The TMF exhibits exceptional, unconventional gas characteristics, such as having a high total organic content (TOC) and low clay content, and it is in the proper maturity window for oil and gas generation. The thickness of the TMF interval ranges from 110 ft to 150 ft across the Jafurah basin [18–20].

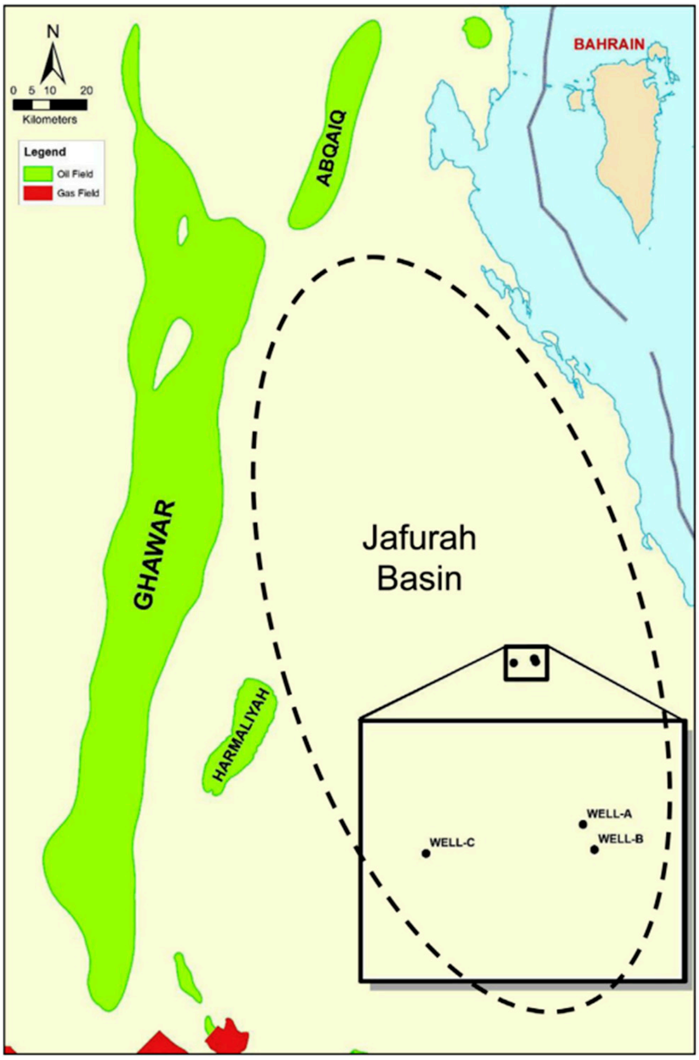

Figure 2. Location map of the estimated outline of Jafurah basin (dashed white line), which is located to the east of the gigantic and prolific Ghawar oil field in Saudi Arabia [20].

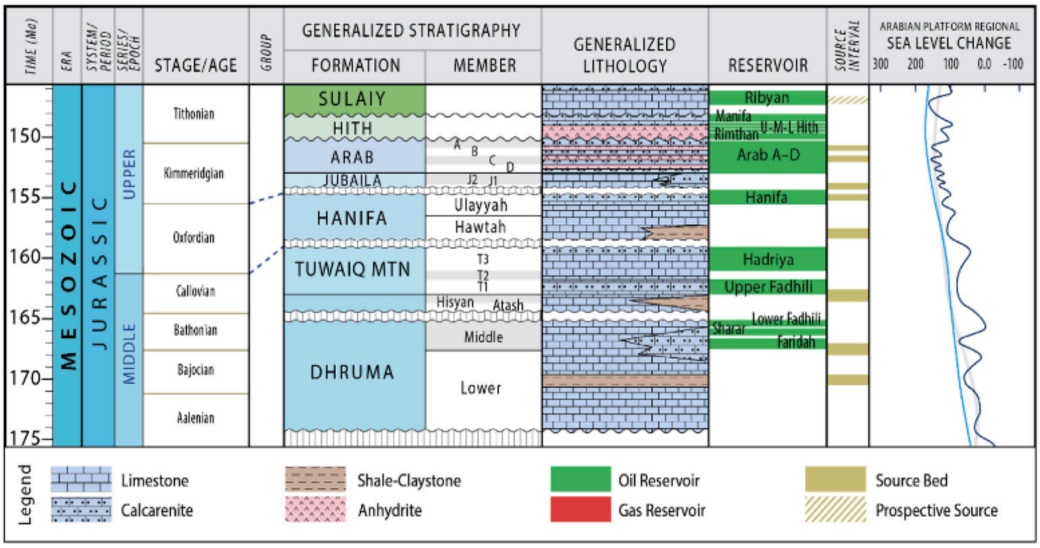

Figure 3. A generalized geological column of the Jurassic period in Jafurah basin including the Tuwaiq Mountain formation [22].

3.1. Petrophysical Evaluation

Wireline logs have been acquired from several vertical pilot wells in the Jafurah basin, which include caliper, spectral gamma ray, sonic, density, and neutron porosity logs as well as their vertical seismic profiles (VSPs) [23]. Figure 4 illustrates a representative calibrated petrophysical evaluation for the TMF [22]. The TMF has been divided into three tiers based on a petrophysical evaluation of the source rock quality, including the total organic carbon (TOC), porosity, permeability, and hydrocarbon saturation. Tier 1 at the bottom represents the most organic-rich interval (with a high maturity) with an average TOC of 7.4% and the most excellent shale characteristics with a high porosity, low clay content, and high hydrocarbon saturation. As illustrated by Figure 4, these excellent properties make Tier 1 the optimum target to place lateral wells. Tier 2 represents rocks of an intermediate source rock quality with an average TOC of 5.9%, while Tier 3 represents rocks of the lowest source rock quality with an average TOC of 3.2%. Isopach maps of the TMF indicate that Tier 3 rocks comprise most of the thickness of the TMF, which ranges between 110 and 150 ft, while Tiers 1 and 2 have a comparable thickness, which ranges between 30 ft and about 40 ft across the Jafurah basin [18].

3.2. Mineralogical Composition

X-Ray diffraction (XRD) technology was used to identify the rock composition and morphology of the TMF. The TMF is mainly composed of organic-rich laminated lime-mud rocks. Table 4 presents a detailed mineralogical composition of the TMF based on XRD measurements from the cores. Calcite is the dominant component with an average of 74% by volume, with a low amount of dolomite, averaging 11% by volume, and a relatively low quartz content, averaging 3% by volume. The total clay content is extremely low with an average of 5%. The high brittle calcite content along with the low-ductility clay content makes the TMF an ideal lithology for effective multistage hydraulic fracturing [18,22].

Scanning electron microscopy (SEM) was utilized to characterize the pore types of the TMF. As illustrated by Figure 5, the internal texture of the organic matter is mainly composed of nanopores. This type of porosity system is the primary pore type in shale gas plays such as the Eagle Ford. SEM images reveal a well-connected organic pore system in the matrix of the TMF with an interconnected porosity around an average of 10%. The shapes of the pores are mostly irregular polygonal to spherical with the main pore sizes being less than 1 µm; the remaining fraction has micro pores greater than 1 µm [20,22].

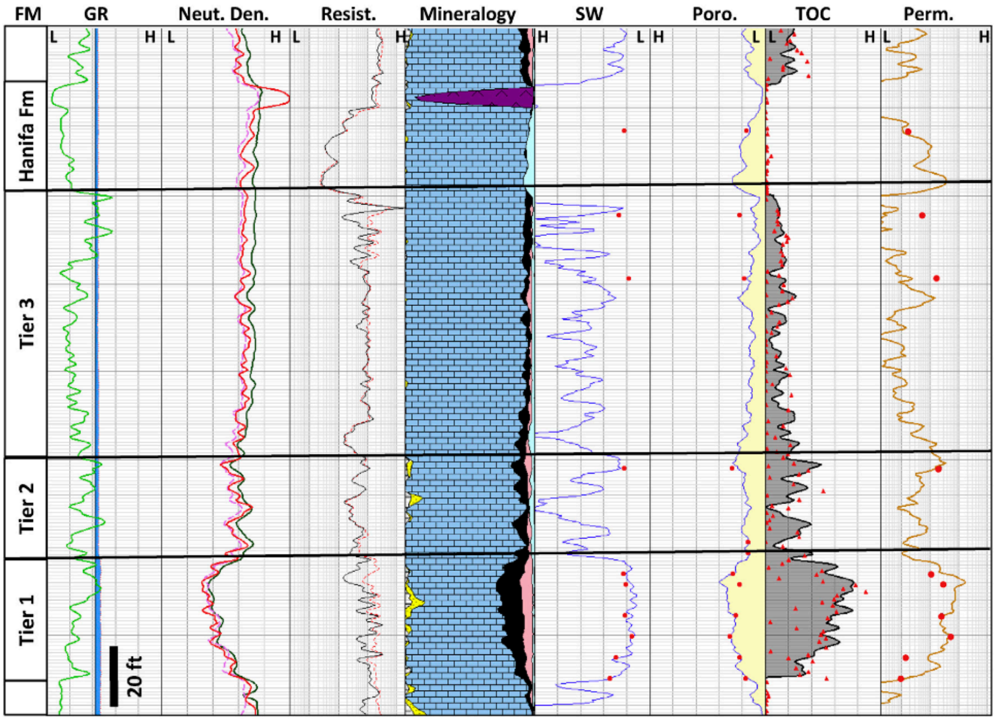

Figure 4. A typical petrophysical model of the Tuwaiq Mountain Formation (TMF) in Jafurah basin. The TMF has been divided into three units in which Tier 1 exhibits the best reservoir characteristics. The red dots represent calibration points with available cores [22].

Table 4. XRD mineral volume fractions for TMF. The max, min, and average are for all three Tiers [22].

Formation Member	Mica	Smectite	Kaolinite	Chlorite	Quartz	Feldspar	Plagioclase	Calcite	Dolomite	Siderite	Pyrite	Anhydrite	Baryte	Gypsum	Halite	Total
Tier 1	1.4	1.1	1.5	0.0	3.3	0.7	1.2	72.5	12.7	0.6	0.9	2.8	0.3	0.3	0.7	100
Tier 2	1.7	1.4	1.7	0.4	2.9	0.7	1.2	73.1	11.8	0.7	1.1	1.9	0.4	0.4	0.8	100
Tier 3	1.6	1.4	1.4	0.9	2.7	0.7	1.2	77.7	8.4	0.7	0.7	1.3	0.3	0.4	0.8	100
Max	2.3	1.9	3.2	1.4	4.8	1.0	2.0	88.9	30.1	0.8	2.4	15.9	0.8	0.7	0.9	
Min	0.9	0.6	0.7	0.0	1.7	0.4	0.8	59.0	1.0	0.4	0.4	0.1	0.1	0.2	0.4	
Ave	1.6	1.3	1.6	0.5	3.0	0.7	1.2	74.3	11.0	0.7	0.9	1.9	0.3	0.3	0.8	100

3.3. Geomechanics Properties

Understanding the geomechanical properties of shale reservoirs is essential for the optimum design of hydraulic fracturing treatments [24]. Experimental studies performed on the elastic and deformational mechanical properties of shale rocks indicate that this type of rock demonstrates a wide range of anisotropic mechanical properties associated with its complicated material composition. Anisotropic mechanical rock tests were completed on representative core samples from Tier 1 of the Tuwaiq Mountain formation. The results show that this zone exhibits a medium level of anisotropy when compared to other highly argillaceous shales. The average static Young's Modulus in the horizontal direction (E_h) is 4.81 Mpsi, whereas in the vertical direction (E_v), it shows a value of 2.92 Mpsi; hence, the static Young's Modulus ratio (E_h/E_v) is about 1.65. For the static Poisson's ratio, the rock exhibits 0.29 in the horizontal direction (ν_h) and 0.21 in the vertical direction (ν_v), whereas the static anisotropic Poisson ratio (ν_h/ν_v) is about 1.38 [22].

Figure 6 illustrates the influence of soft material (clay and kerogene) content on the static anisotropy E_h/E_v of various shale gas plays [25]. Based on this work, it is demonstrated that the static anisotropy for the Young's Modulus (E_h/E_v) is directly related to the content of the soft material (clay and kerogene). The measurement for Tier 1 of the Tuwaiq Mountain Formation is relatively comparable to that of the Eagle Ford play.

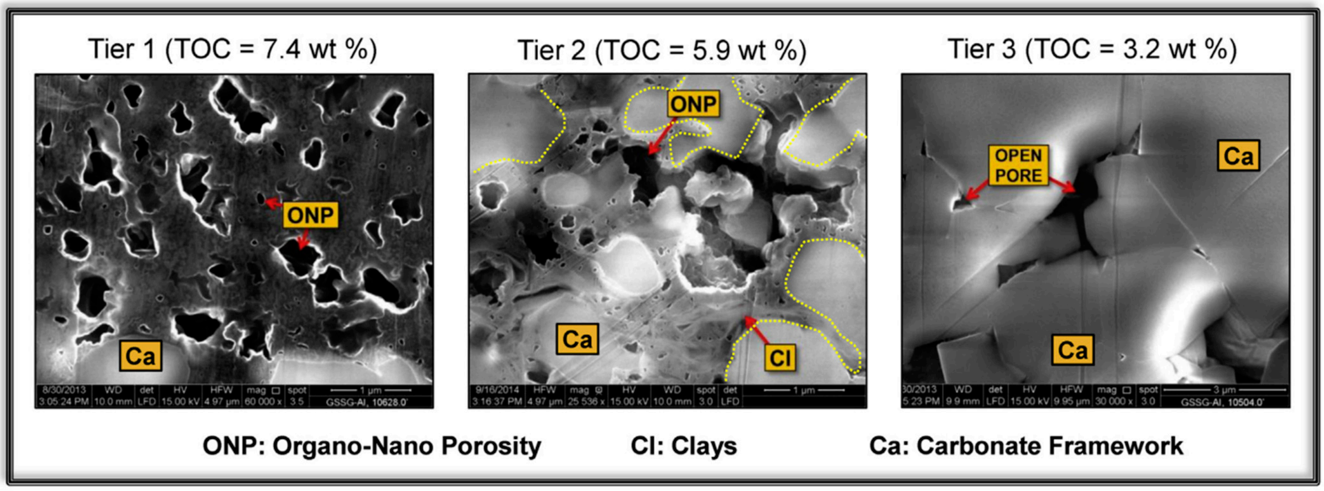

Figure 5. SEM images illustrate the organic porosity distribution, with Tier 1 showing the highest organic porosity [22].

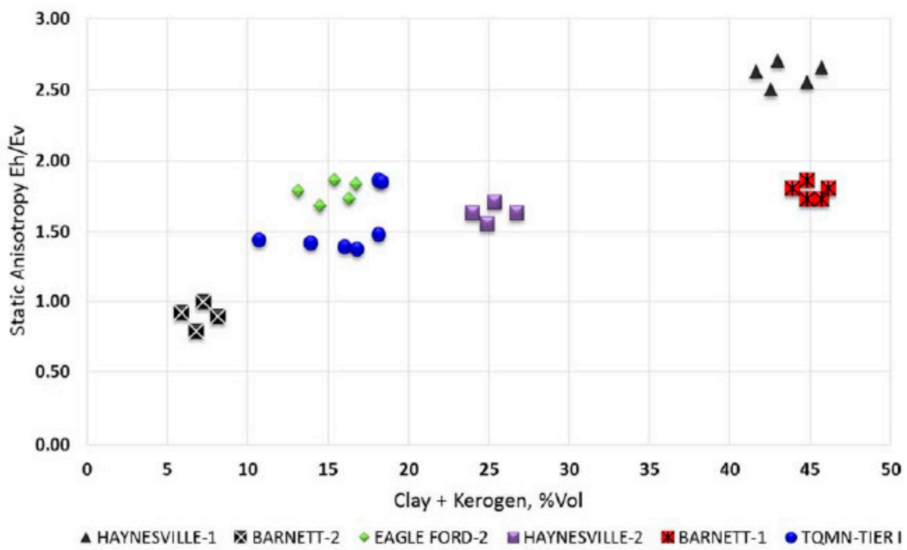

Figure 6. Effect of clay and kerogen content on the static anisotropy E_h/E_v. Data for Tuwaiq Mountain Formation are shown in blue [22].

Based on diagnostic fracture injectivity tests (DFITs), the pore pressure in the TMF is about 0.7 psi/ft at a reservoir target depth of 10,000 ft. The local stress regime is characterized by strike–slip conditions, with σ_v = 1.1 psi/ft, σ_{Hmax} = 1.2 psi/ft, and σ_{hmin} = 0.96 psi/ft. The direction of the minimum regional stress is NW, prompting for field development with lateral wells extending in the NW–SE direction [23].

4. Estimation of Elastic Properties of Jafurah TMF

We employ the XRD data (see Table 4) to estimate the velocity and elastic properties of the TMF formation and conduct a sensitivity analysis over different parameters. Table 5 shows the average mineral volume fractions taken from several TMF samples across Tier 1, Tier 2, and Tier 3 intervals. Here, we use the average of all three intervals to obtain an estimate of the formation's elastic properties. This table shows that calcite is the dominant mineral in the TMF formation (with an average of 74.3%) followed by dolomite (with an average of 11%). Additionally, the presence of clay minerals (e.g., mica, smectite, kaolinite, chlorite) is about 5%, which is minimal. This means that the anisotropic nature of the TMF formation as suggested by previous studies is not due to the lamination caused by clay. Most likely, the anisotropy is due to the existence of natural fractures, which are commonly observed in brittle carbonate rocks. The abundance of calcite and low percentage of clay causes the formation to be brittle, and this is indeed the reason the TMF formation is a good target for hydraulic fracturing, as the prime stimulation technology to enhance production is found in this formation.

Table 5. XRD mineral volume fractions for TMF. The max, min, and average are for all three Tiers (after [22]).

Formation Member	Mica	Smectite	Kaolinite	Chlorite	Quartz	Feldspar	Plagioclase	Calcite	Dolomite	Siderite	Pyrite	Anhydrite	Baryte	Gypsum	Halite	Total
Tier 1	1.4	1.1	1.5	0.0	3.3	0.7	1.2	72.5	12.7	0.6	0.9	2.8	0.3	0.3	0.7	100
Tier 2	1.7	1.4	1.7	0.4	2.9	0.7	1.2	73.1	11.8	0.7	1.1	1.9	0.4	0.4	0.8	100
Tier 3	1.6	1.4	1.4	0.9	2.7	0.7	1.2	77.7	8.4	0.7	0.7	1.3	0.3	0.4	0.8	100
Max	2.3	1.9	3.2	1.4	4.8	1.0	2.0	88.9	30.1	0.8	2.4	15.9	0.8	0.7	0.9	
Min	0.9	0.6	0.7	0.0	1.7	0.4	0.8	59.0	1.0	0.4	0.4	0.1	0.1	0.2	0.4	
Ave	1.6	1.3	1.6	0.5	3.0	0.7	1.2	74.3	11.0	0.7	0.9	1.9	0.3	0.3	0.8	100

It is to be noted that in Table 5, kerogen is not included in the mineralogy, as XRD data cannot detect kerogen. The TMF is organically rich, and the effect of the TOC or kerogen is substantial on the formation's properties. We use the relationship between the TOC and kerogen to estimate the kerogen percentage. The atomic ratios of hydrogen to carbon (HCAR) for kerogen types 1, 2, and 3 during diagenesis are 1.25, 1.34, and 1.48, respectively. At the end of the catagenesis process, the HCAR for the three kerogen types are 1.20, 1.19, and 1.18, respectively [26]. The average weight percentage (wt%) of the TOC in the TMF (all tiers) is 4.9%. As discussed previously, the TMF has mainly kerogen type 2. To determine the organic maturity stage of this formation, we use Table 6, which shows the genetic classification of bitumen based on the organic maturity stage, vitrinite reflectance (R_0), and hydrocarbon generation window [27]. The average vitrinite reflectance (R_0) for the TMF formation is 1.39%. This places the kerogen type of the TMF formation under the catagenesis stage. Therefore, the conversion factor for the TOC to kerogen for use is 1.19. Thus, the estimated weight fraction of kerogen is $4.9\% \times 1.19 \approx 6\%$.

While the weight fraction and volume fraction for most minerals with an average density of 2.6 gr/cc are nearly the same, this is not the case for kerogen. As stated by [28], because the organic matter that becomes kerogen is deposited at the same time as the inorganic rock mineral grains, it is crucial to consider that the kerogen occupies a significantly larger volume percentage (vol%) than is indicated by the weight percentage (wt%) measurement; this is because of the low grain density of the organic matter (typically 1.1–1.4 g/cc) compared to that of common rock-forming minerals (2.6–2.8 g/cc). Therefore, we use a conversion factor of 2 to estimate the vol% of kerogen from its wt%; hence, the kerogen vol fraction is estimated to be 12%. In the published reports (refer to Figure 7), the average volume fractions of kerogen and clay together for the TMF formation are given as 10–20%. Considering that the amount of clay is about 5% (see the last row in Table 5 for the total of the four clay minerals), this estimate appears to be well within the expected range. The porosity of kerogen is generally very low and, on average, around 5%, which will have a negligible effect on the total porosity of the formation and can be ignored.

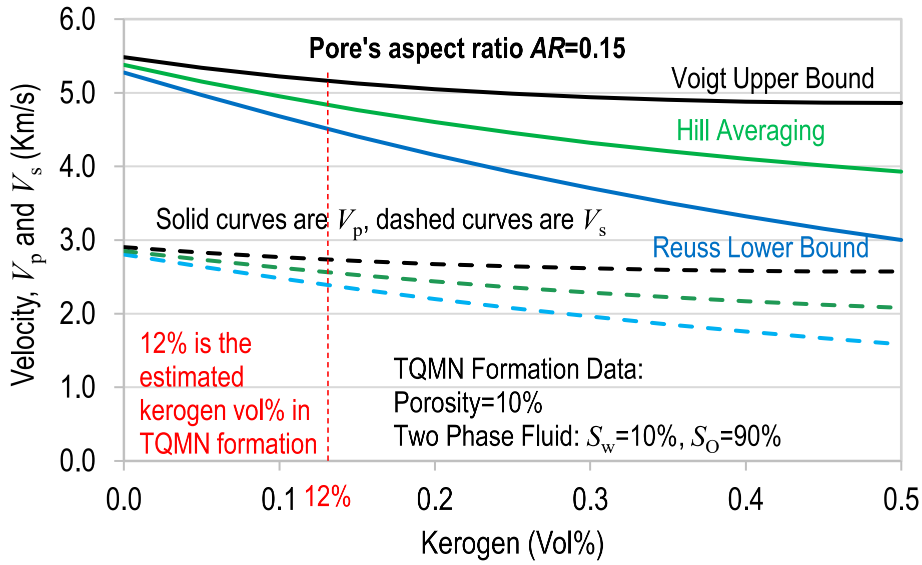

Figure 7. Estimated compressional (V_P) and shear (V_P) velocities for TMF formation using (Voigt) upper-bound, (Reuss) lower-bound, and (Hill) average rock physics models, assuming average pore aspect ratio of AR = 0.15. Estimated vol% of kerogen for the formation is shown as 12% vertical dashed line.

Table 6. Genetic classification of bitumen based on the organic maturity stage, vitrinite reflectance (R0), and hydrocarbon generation window (after [27,29]).

Maturity Stages	**Diagenesis Ro < 0.5%**		**Catagenesis 0.5% < Ro < 2.0%**		
Hydrocarbon generation window	Pre-oil generation (immature) Ro < 0.5%	Incipient-oil generation (early oil) Ro ~ 0.5–0.7%	Primary-oil generation (peak oil) Ro ~ 0.7–1.0%	Post-oil generation (late oil/wet gas) Ro ~ 1.0–1.4%	Dry gas generation (overmature) Ro > 1.4%
Liquid Bitumen	Bituminite/ Amorphinite	Bitumen (Exsudatinite)	Asphalt	Waxes	Hydrocarbon residue
Solid Bitumen	Diagenetic solid bitumen	Initial-oil solid bitumen	Primary-oil solid bitumen	Late-oil solid bitumen	Pyrobitumen

Including kerogen into the mineral composition of the TMF formation, the volume fractions of the minerals in the last row of Table 5 should be divided by a factor of 1.12. Table 7 shows the results. These values are used in the next section to estimate the velocity and elastic properties of the TMF formation using Helm's correlations.

Table 7. Mineral volume fractions for TMF, including kerogen.

Mica	Smectite	Kaolinite	Chlorite	Quartz	Feldspar	Plagioclase	Calcite	Dolomite	Siderite	Pyrite	Anhydrite	Baryte	Gypsum	Halite	Kerogen	Total
1.4	1.1	1.4	0.4	2.6	0.6	1.0	66.0	9.5	0.6	0.8	1.7	0.2	0.2	0.5	12.0	100

The DEM-based correlations developed by [9] were employed to estimate the velocity and elastic parameters of the TMF formation. Here, we assumed that the early stage of production is when oil is the dominant producing fluid; hence, two-phase fluids of water and oil were considered. As the water saturation in the TMF is low, a water saturation of Sw = 10% was considered. Figure 7 shows the change in the compressional and shear velocities as a function of the kerogen volume fraction. The results are plotted based on (Voigt) upper-bound, (Reuss) lower-bound, and (Hill) average rock physics models. In this example, the pore's aspect ratio of 0.15 was assumed to be the average pore geometry. From this plot, it is observed that, as expected, the compressional velocities are higher than the shear velocities, and the velocities decrease as the kerogen occupies more of the volume of the rock. Moreover, the plots show that the difference between the Voigt, Reuss, and Hill models is less as the kerogen volume decreases.

The 12% vertical dashed line shows the estimated average kerogen volume fraction in the TMF formation, as discussed in the previous section. This corresponds to average compressional and shear velocities of 4.85 Km/s and 2.60 Km/s, respectively. Assuming that the average pore aspect ratios of the TMF correspond to interparticle (intercrystal) pores with AR = 0.15, these velocities represent the average values.

Figure 8 represents the plots of both the compressional (top) and shear (bottom) velocities estimated based on the Hill average, as a function of varying pore aspect ratios. It is seen that as the aspect ratio increases, i.e., changing from crack-type to more spherical pore geometries, the velocity increases. This is indeed due to the fact that the crack pores have larger lengths and surface areas to affect the velocity. It is interesting to note that the effect of the pore geometry is less influencial when the aspect ratio goes above approximately 0.15. Additionally, the results suggest that, while increasing the kerogen volume fraction reduces the velocity, this effect is minimal for crack-type pores than larger pores' aspect ratios. The results show that depending on the pore's aspect ratio, the compressional and shear velocities at a 12% kerogen volume fraction change from 2.0 to 5.4 Km/s and 1.0 to 2.9 Km/s, respectively.

Figure 9 presents the plots of the bulk, K, (top) and shear, μ, (bottom) moduli, which are calculated using Equation (3) and from the velocity plots of Figure 8. Similar trends for the velocities are observed for the change in bulk and shear moduli with respect to increasing kerogen and pore ARs. At a 12% kerogen volume fraction, the bulk and shear moduli vary depending on the pore Ars from 1.0 to 6.0 Mpsi and 0.3 to 3.0 Mpsi, respectively.

Figure 10 represents the Young's modulus (E) variations over time. The top plot shows estimated values based on the Voigt, Reuss, and Hill models, assuming AR = 0.15 for the pores. The bottom plot shows the results as a function of the kerogen vol% and different pores' ARs. At a 12% kerogen vol%, the Young's modulus changes from 5.5 to 6.2 and 7 Mpsi, corresponding to the Reuss, Hill, and Voigt models, respectively. Moreover, the Young's modulus varies between 0.9 and 7.9 Mpsi at a 12% kerogen vol% for the crack to moldic pore types.

The SEM analysis of the TMF formation showed that the major pores are interparticle (see Figure 5) with an average of pore AR of 0.10–0.15. Figure 10 (bottom) translates to a Young's modulus of 4.6–4.8 Mpsi at a 12% kerogen volume fraction. The limited published data report the Young's modulus of the TMF formation as 3.8 Mpsi [30]. On another occasion, the anisotropic Young's modulus of the TMF has been reported to be 4.81 Mpsi parallel to the layering plane (E_H) and 2.91 Mpsi perpendicular to the layering plane (E_v) [22]. With respect to all the uncertainties of XRD data that can be caused by the complex nature of shale formations, the experimental challenges of the reported values for the Young's modulus and the scale effect are within a reasonable range. However, the use of the presented inclusion-based rock physics correlations allows us to estimate the elastic and velocity properties for a wide range of kerogen volume fractions, as well as pore geometries. The presented models can also be used to conduct a sensitivity analysis for other parameters, such as the fluid types, saturations, and porosity changes, to estimate the velocity and elastic properties as the reservoir is depleted and evolves over time.

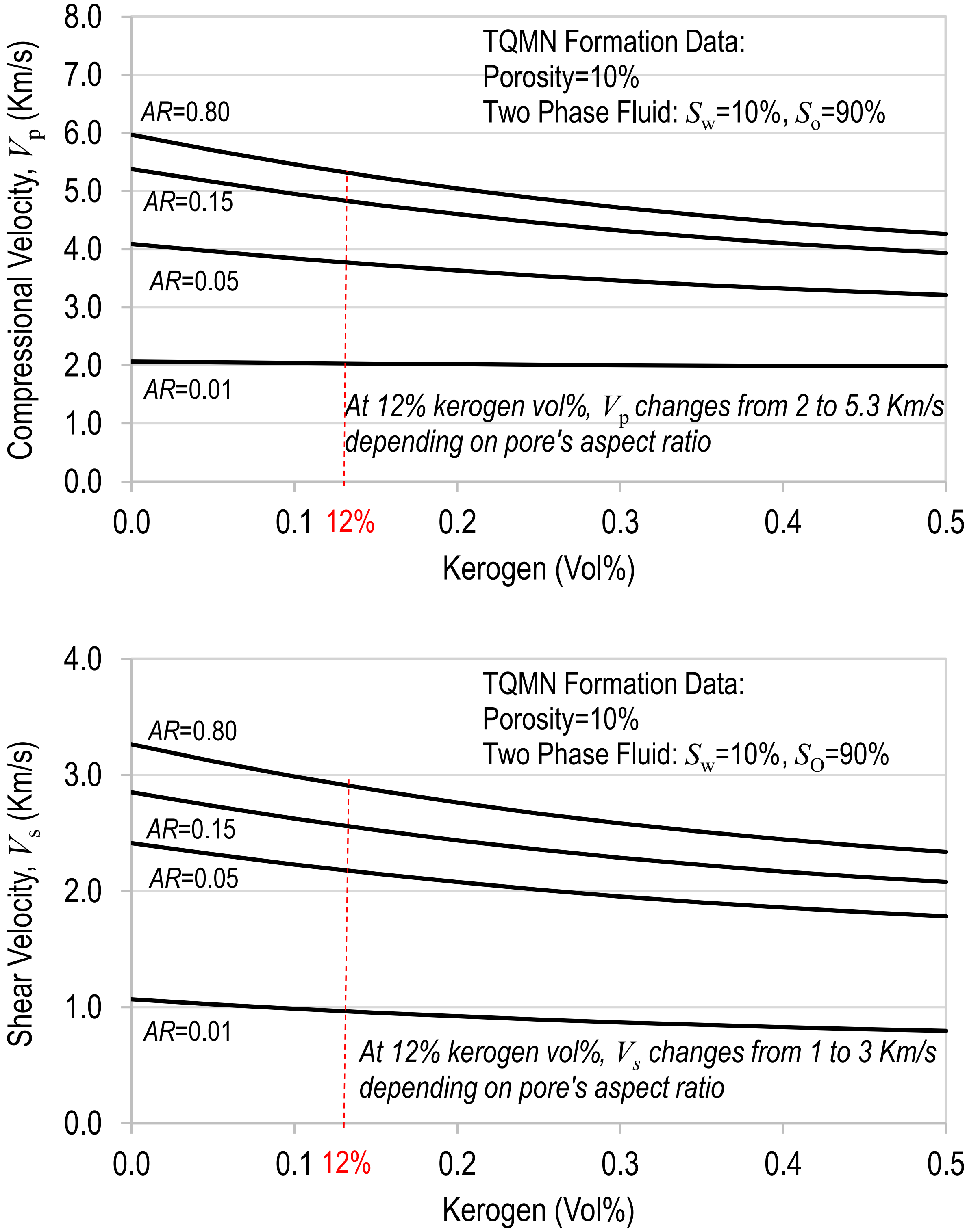

Figure 8. Estimated compressional, V_p, (**top**) and shear, V_s, (**bottom**) velocities for TMF formation based on Hill average rock physics model, assuming different pore aspect ratios.

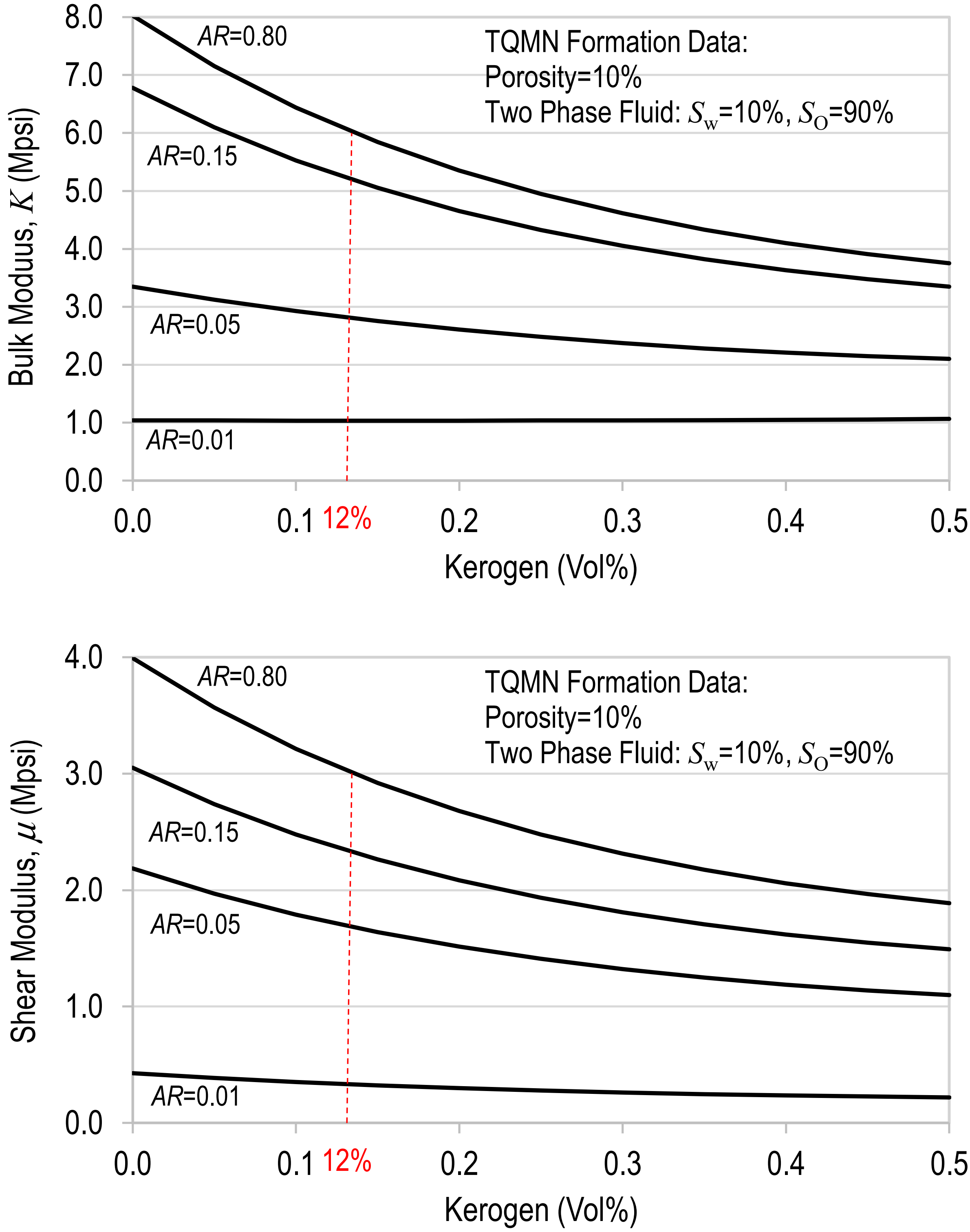

Figure 9. Estimated bulk, K (**top**) and shear (**bottom**) moduli for TMF formation based on Hill average rock physics model, assuming different pore aspect ratios.

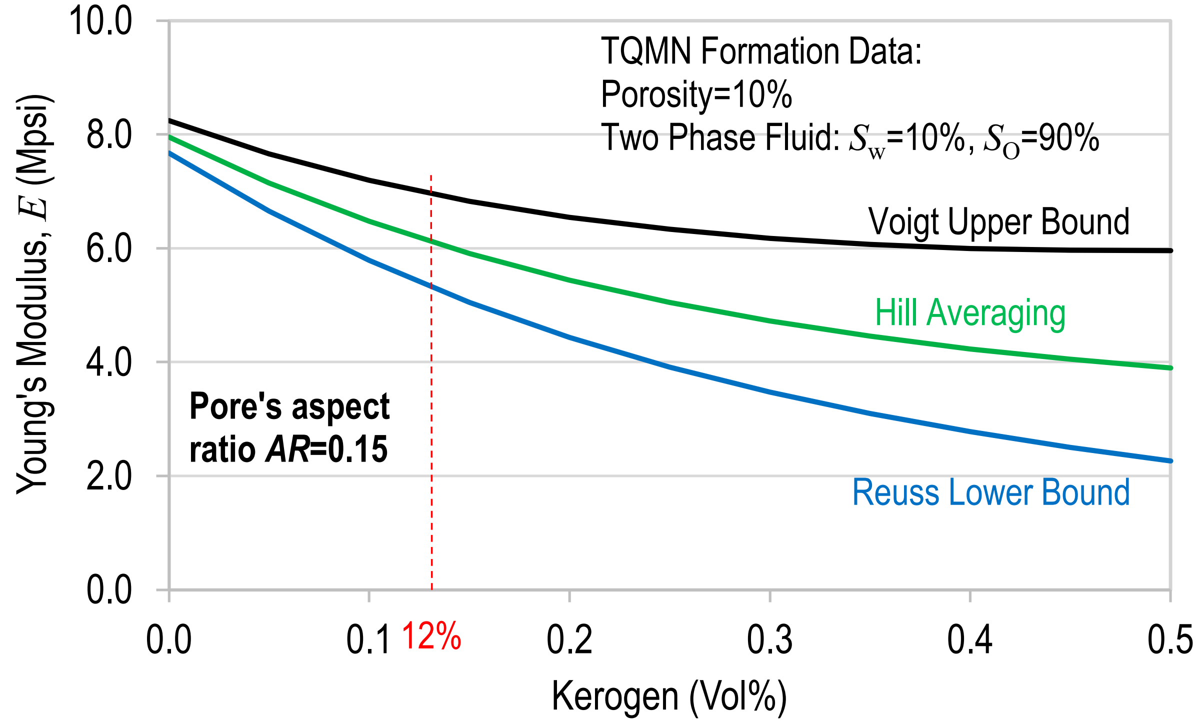

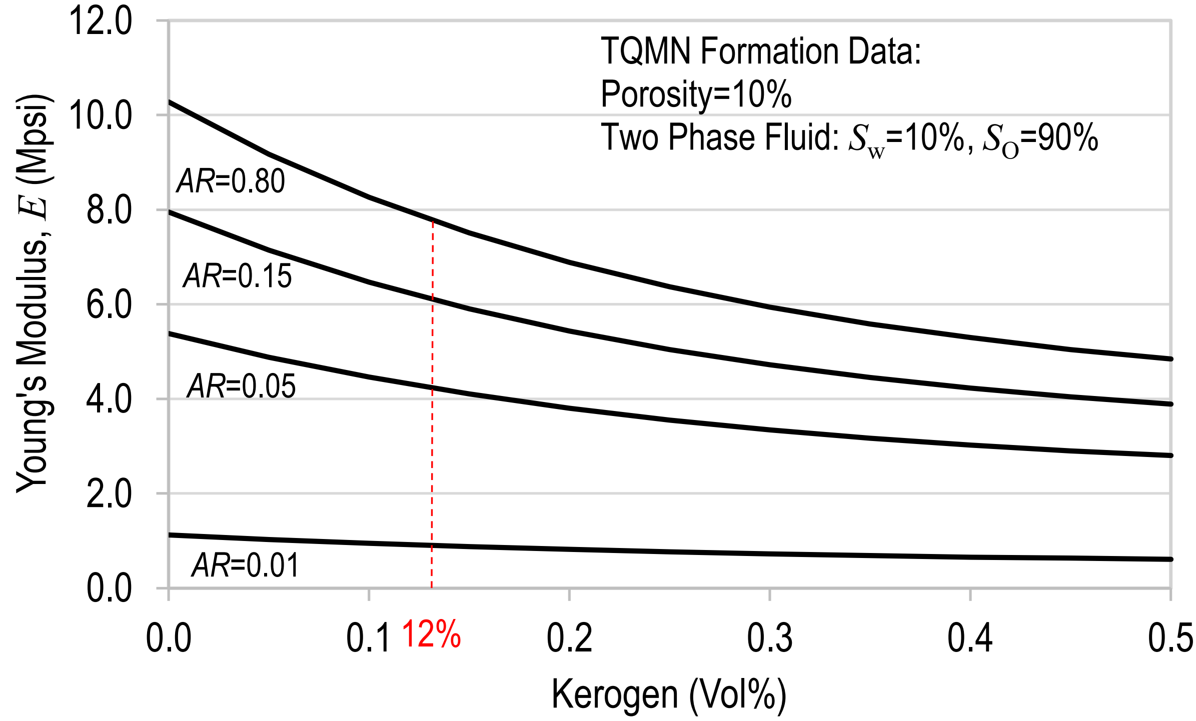

Figure 10. Estimated Young's modulus (E) for TMF formation based on Voigt, Reuss and Hill average rock physics models (**top**) and assuming different pore aspect ratios using Hill average model (**bottom**).

5. Estimation of the Brittleness Index

In hydraulic fracturing, the idea is to shatter the rock near the propagating fracture through high fluid pressure. The ability to generate larger volume of cracks near the propagating fracture depends on the rock's stiffness. In general, the larger the Young's Modulus and the smaller the Poisson's ratio, the more impactful the fracturing operation will be, and a larger volume of rock near the fracture will be stimulated. This volume is called the stimulated reservoir volume (SRV) [31–33].

The brittleness index (BI) is a parameter which is used to quantitatively rank the frac-ability of a formation as a measure of its elastic properties. The BI is usually measured based on the stress–stain curve, which is plotted from laboratory triaxial stress testing. The amount of energy released before and after the peak strength are used to define the brittleness [34]. An indirect measurement of the BI is performed from the XRD lab results, core data, petrophysical log responses, or seismic data. Of course, the BI estimated from each of these methods is interpreted with their measured scales and conditions.

These formulations were used by [24,27] to measure the BI of the Eagle Ford formation based on XRD; the mineralogical composition of the rock ($BI_{mineral}$) and elastic properties ($BI_{elastic}$) of the core samples are given as follows [24,27]:

$$BI_{mineral} = \frac{Carbonate}{Carbonate + Quartz + Clay} \tag{14}$$

$$BI_{elastic} = 0.5\left(\frac{E(0.8-\phi)}{8-1} + \frac{\nu - 0.4}{0.15-0.4}\right) \times 100 \tag{15}$$

In general, quartz is considered a stiffening mineral for most rocks, which increases the brittleness index, so it is expected to appear on the numerator of the fraction in Equation (14). However, according to [24,27], "QFP is the common component in the Eagle Ford formation, and it is often considered as the stiff phase for many reservoir rocks. However, in the Eagle Ford, feldspar is rare, and content of pyrite is much less than quartz content. Quartz mineral is more abundant in mud-supported facies than grain-supported facies. In mudstone and wackestone, quartz commonly exists as authigenic cements or microcrystalline cement that fill porosity in the rock matrix in the Eagle Ford samples. Apparently, for the Eagle Ford, quartz cement that is associated with clays or among coccolith fragments do not serve as a load-bearing framework. Thus, with increasing quartz cements distributing throughout the matrix, stiff phase in the rock such as carbonate decreases, elastic moduli-based brittleness index therefore decreases" [24,27].

We adopted Equations (14) and (15) in this study in order to compare the results of the TMF's Young's moduli and brittleness behavior with those of the Eagle Ford. Due to the lack of access to the data from the TMF, except for some XRD data, we could not do a direct estimation of the BI based on the triaxial testing results on the core samples from the TMF or using log or seismic data.

To calculate the $BI_{mineral}$ variation in the TMF with respect to the mineral type and elastic properties, we used the XRD data of the TMF (see Table 4). Calcite and dolomite were considered carbonate minerals, while calcite constituted the primary volume of the TMF. Additionally, the quartz content is very low in the TMF (with an average of 3%), so it does not affect the results of the BI estimation, contrary to that of Eagle Ford, in which the quartz content is relatively large. As discussed before, the clay content (illite, chlorite, and smectite) of the TMF is small and less than 5% on average. However, the average kerogen, as estimated previously, is 12%. Kerogen may be added as a ductile mineral in the denominator of Equation (14) to see the impact of the TOC on the brittleness of the formation.

To calculate $BI_{elastic}$ considering the formation's mineralogy, we used the estimated Young's modulus from inclusion-based rock physics correlations (previous section). The

Poisson's ratio was calculated from its elastic relationship with the Young's modulus and shear modulus as follows:

$$E = 2\mu(1 + v) \tag{16}$$

If the Young's modulus and Poisson's ratio are estimated using correlations with the compressional and shear sonic and density petrophysical logs, they are called dynamic moduli [34]. Dynamic moduli are usually larger than static moduli, which are measured from triaxial stress lab measurements. Dynamic moduli must be transformed into static values by comparing them to lab data. Moreover, seismic-driven elastic moduli are known as dynamic moduli as they are velocity-based values. As in this study, we did not have core, log, or seismic data, and we derived the Young's moduli from the mineralogical composition and Poisson's ratio using its elastic relationship with the Young's and shear moduli; these are closer to the static moduli. From the limited data published on the TMF, we determined the following ratios between the static and dynamic Young's moduli and Poisson's ratio:

$$\frac{E_{dyn}}{E_{sta}} = 1.30 - 1.75 \tag{17}$$

$$\frac{v_{dyn}}{v_{sta}} = 0.76 - 1.03 \tag{18}$$

However, it is very common to consider similar values for the dynamic and static Poisson's ratio [27]. In the following, we present examples of the cross-correlations of the TMF elastic moduli and the BI with formation mineralogy. Figure 11 shows the change in the Young's modulus and the $BI_{elastic}$ as a function of the clay content. In general, an increase in clay volume results in a decrease in both of these parameters. Additionally, moving from Tier 1 to Tier 2 and Tier 3, the Young's modulus and BI are reduced, which is expected, as the amount of calcite minerals is less. The Young's modulus and $BI_{elastic}$ are generally changing as a function of the clay content with a range of 7.3–8.3 Mpsi and 0.55–0.61, respectively.

If a constant kerogen amount of 12% is added in the denominator of Equation (13) and the calculation is repeated, the results show the same trend as is shown in Figure 12; however, the range of the Young's modulus and $BI_{elastic}$ changes to 5.7–6.4 Mpsi and 0.47–0.52, respectively. In fact, the addition of the kerogen, as expected, reduces the stiffness properties of the formation.

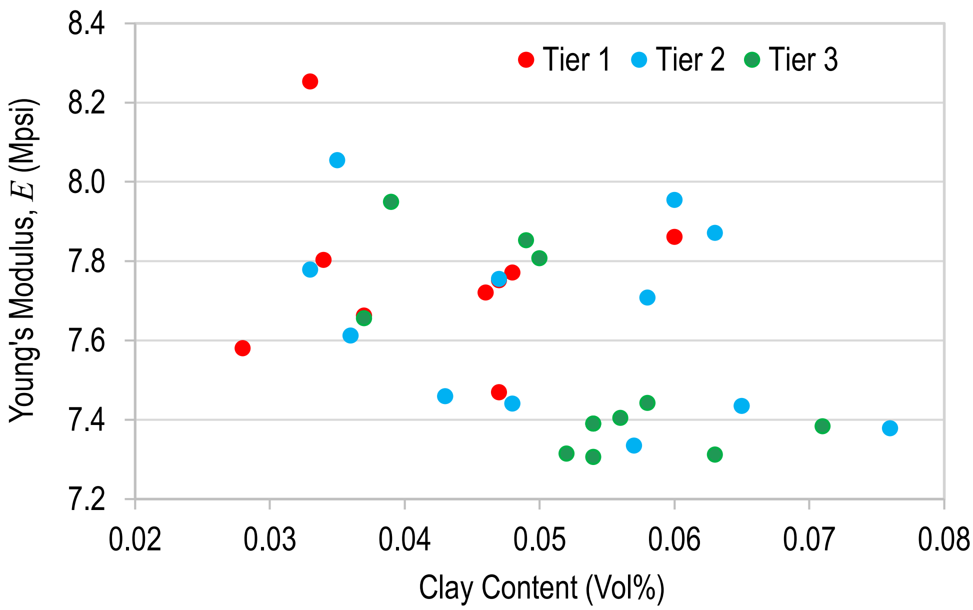

Figure 11. *Cont.*

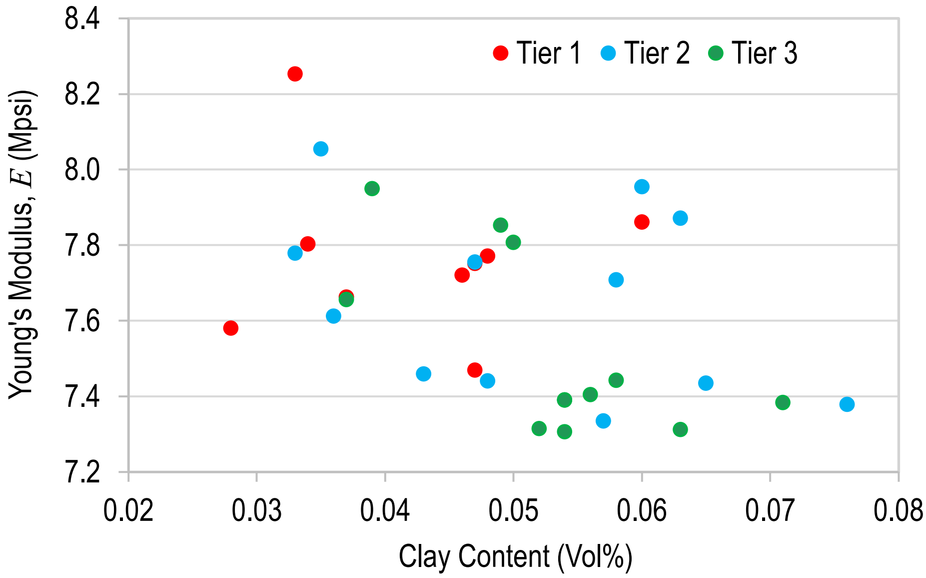

Figure 11. Change of Young's modulus (**top**) and elastic brittleness index (**bottom**) as a function of clay content for TMF.

Figure 12 shows the variations of the Young's modulus and $BI_{elastic}$ as a function of carbonate content. While the data are very scattered, an increasing trend is observed for the two parameters when the carbonate minerals increase. Due to its larger calcite content, data belonging to the Tier 1 category show slightly more pronounced elastic and brittleness behavior compared to those of the Tier 2 and Tier 3 categories.

Plots of $BI_{elastic}$ as a function of the Young's modulus are presented in Figure 13. The inclusion of kerogen and clay as mineral constituents is considered during the calculation of the BI. The top plot shows the trendlines for each TMF's tier. It is evident that Tier 1 has a larger BI than that of Tier 2 and Tier 3. The bottom plot of Figure 13 presents the overall trend of $BI_{elastic}$ with respect to the Young's modulus for all three tiers of the TMF for two cases of clay and clay + kerogen which are included in the mineral composition of the formation. It is clear that adding kerogen reduces the brittleness and Young's modulus. The following correlations are extracted from Figure 13:

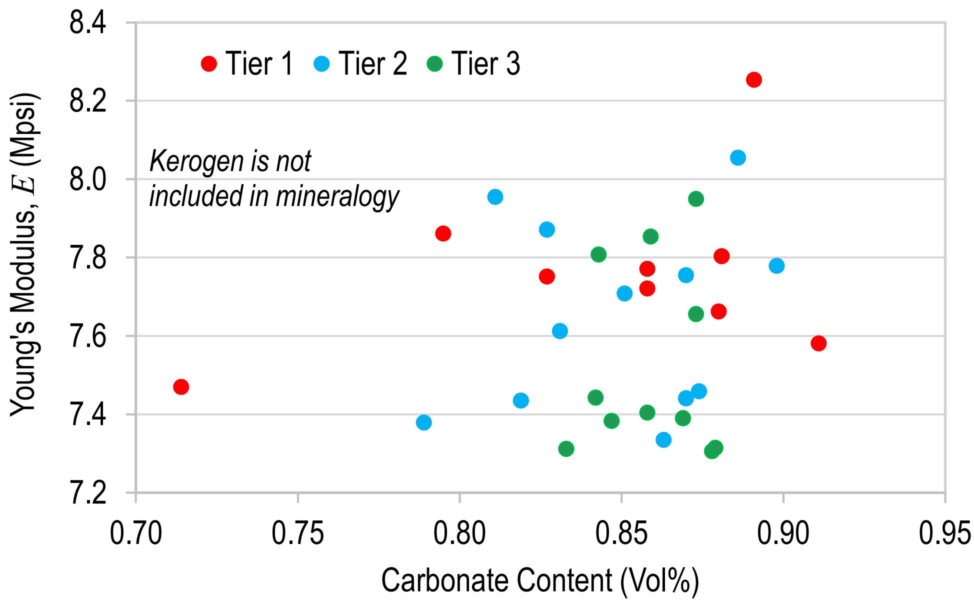

Figure 12. *Cont.*

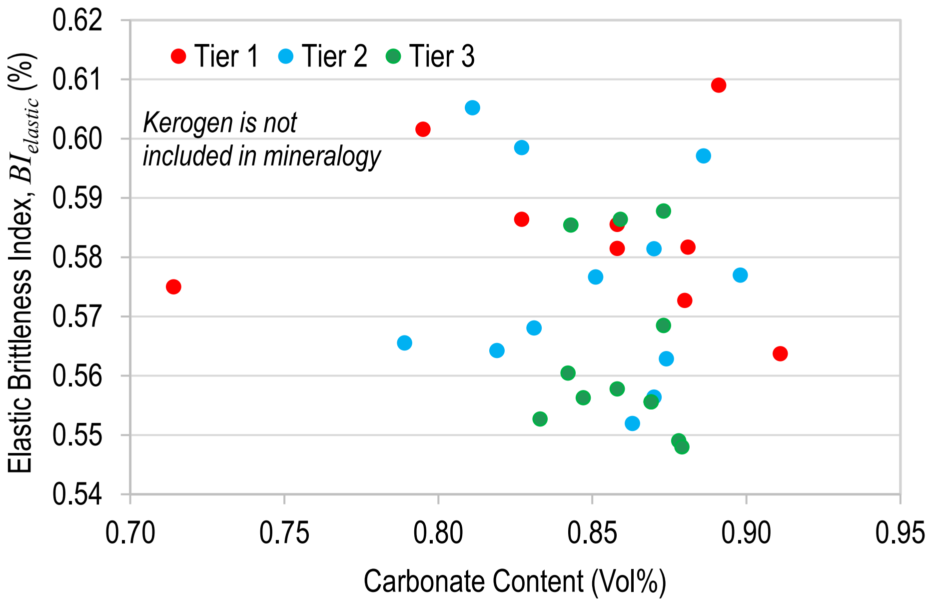

Figure 12. Change of Young's modulus (**top**) and elastic brittleness index (**bottom**) as a function of carbonate content for TMF.

$$EI_{elastic} = 0.057E + 0.155 \;\; \text{Tier 1} \;\; (\text{clay} + \text{kerogen}) \tag{19}$$

$$EI_{elastic} = 0.047E + 0.210 \;\; \text{Tier 2} \;\; (\text{clay} + \text{kerogen}) \tag{20}$$

$$EI_{elastic} = 0.052E + 0.175 \;\; \text{Tier 3} \;\; (\text{clay} + \text{kerogen}) \tag{21}$$

$$EI_{elastic} = 0.066E + 0.067 \;\; \text{All Tiers} \;\; (\text{clay}) \tag{22}$$

$$EI_{elastic} = 0.059E + 0.136 \;\; \text{All Tiers} \;\; (\text{clay} + \text{kerogen}) \tag{23}$$

The top plot of Figure 14 shows the variation in the Young's modulus versus Poisson's ratio. Here, kerogen is not added to the mineral content. The results show that the Poisson's ratio is changing within a tiny range of 0.295–0.310, with the following linear relationship presenting the variation:

$$E = -42.85v + 20.66 \;\; \text{All Tiers} \;\; (\text{clay}) \tag{24}$$

A similar trend is observed when kerogen is added to the mineral composition with the following relationship showing the change in the Young's modulus as a function of the Poisson's ratio:

$$E = -35.41v + 16.77 \;\; \text{All Tiers} \;\; (\text{clay} + \text{kerogen}) \tag{25}$$

Figure 14 (bottom) shows the plot of $BI_{elastic}$ versus the Poisson's ratio for two cases of clay and clay + kerogen as part of the TMF mineral composition. It is seen that, in general, the BI is reduced as the Poisson's ratio increases. When kerogen is part of the mineralogy, the BI becomes lower. The following linear correlations are the best fits for the data from all three tiers:

$$E = -4.143v + 1.833 \;\; \text{All Tiers} \;\; (\text{clay}) \tag{26}$$

$$E = -2.911v + 1.377 \;\; \text{All Tiers} \;\; (\text{clay} + \text{kerogen}) \tag{27}$$

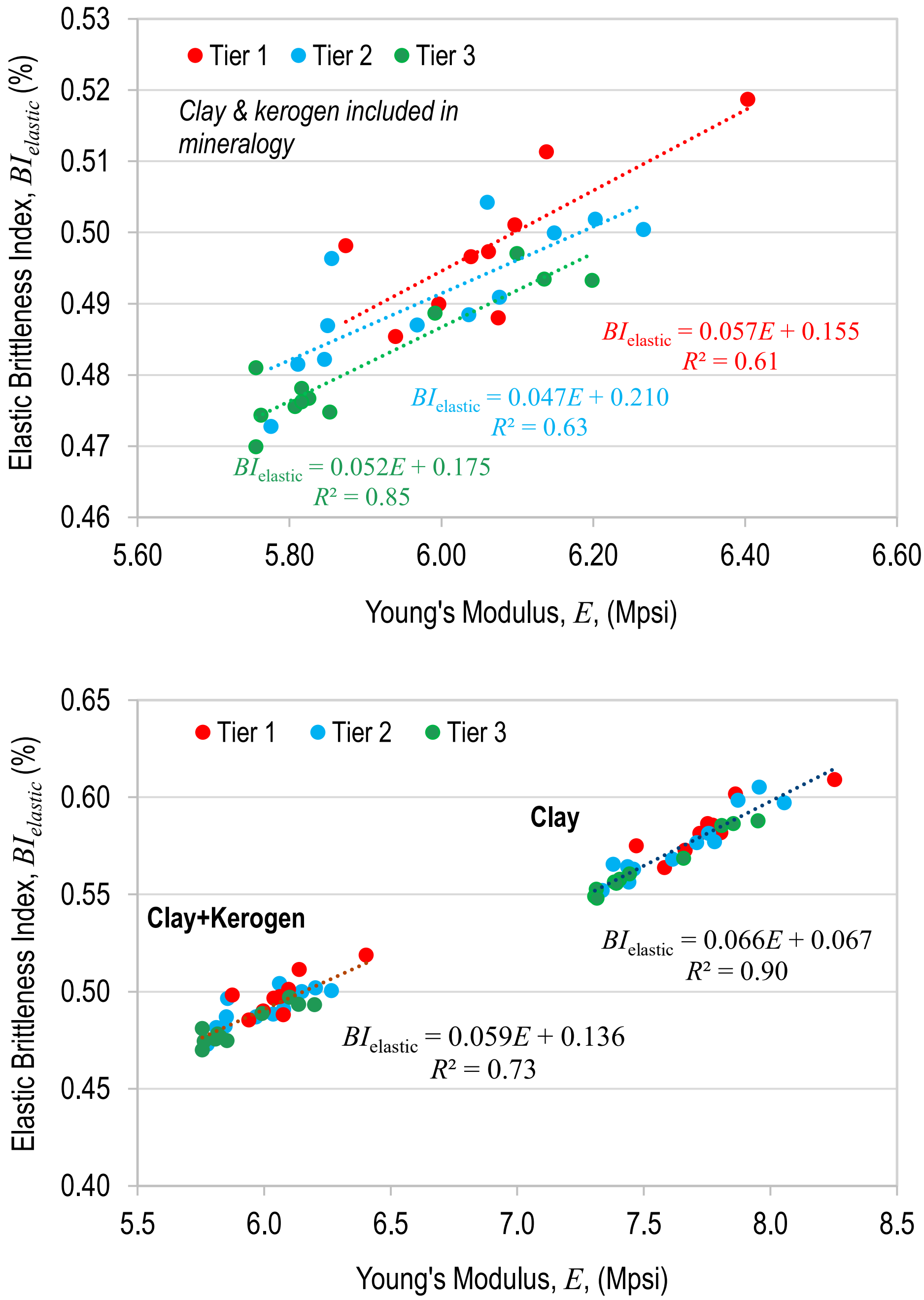

Figure 13. Relationship between elastic brittleness index for each TMF tier when kerogen is considered in mineralogy (**top**) and the overall trend for all three tiers when only clay and both clay and kerogen are included in mineralogy (**bottom**).

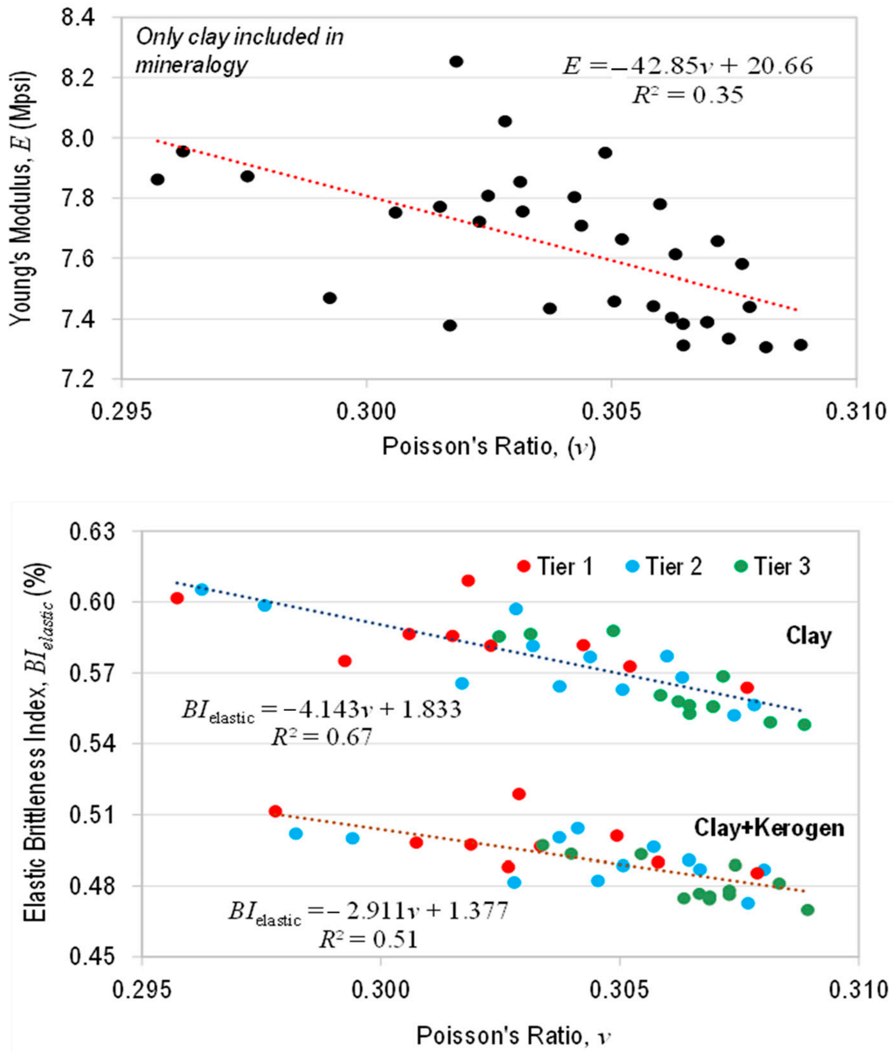

Figure 14. Change in Young's modulus as a function of Poisson's ratio (**top**). Relationships between elastic Young's modulus and Poisson's ratio for all three TMF tiers when only clay and when clay and kerogen are included as mineral constituents (**bottom**).

Figure 15 (top plot) shows the changes in the mineral brittleness index $BI_{mineral}$ versus the Young's modulus for Tier 1, 2, and 3 of the TMF formation in which two cases of only clay and clay + kerogen included in the mineral composition. The results show that when the clay is added to the mineral composition, the $BI_{mineral}$ is reduced, similar to $BI_{elastic}$. Figure 15 (bottom) shows the cross-correlation of the $BI_{elastic}$ versus $BI_{mineral}$. In general, it is observed that the $BI_{mineral}$ is larger than $BI_{elastic}$.

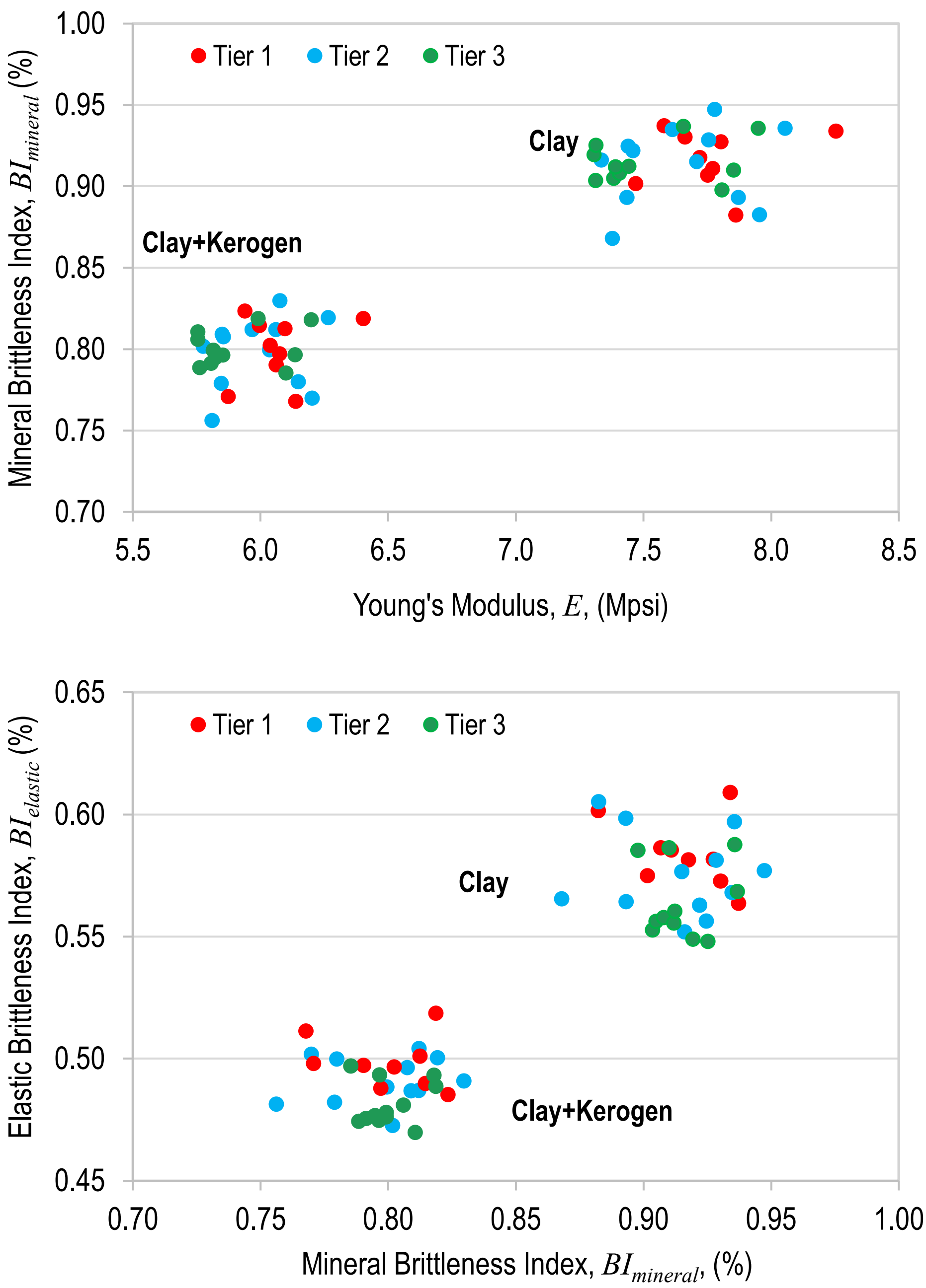

Figure 15. Change in mineral brittleness index as a function of Young's modulus for TMF tiers for two cases of only clay and clay and kerogen as part of the mineral content (**top**). Relationship between elastic and mineral brittleness indexes for TMF tiers for two cases of only clay and clay and kerogen as part of the mineral content (**bottom**).

6. Tuwaiq Mountain Formation vs. Eagle Ford

Xu 2019 [24] conducted a study on the brittleness index of Eagle Ford shale. He used both direct and indirect methods. According to his results, overall, the brittleness indices of the Eagle Ford shale estimated from indirect methods (i.e., mineral and elastic methods) varied from 0.47 to 0.96. The BI_{mineral} varied from 0.72 to 0.96 and the BI_{elastic} ranged from 0.53 to 0.72 [24].

Table 8 summarizes the brittleness indices for the Eagle Ford and TMF, which show a comparable range.

Table 8. Comparison of mineral and elastic brittleness indices for Eagle Ford and TMF.

	Eagle Ford [24]	TMF
BI_{mineral}	0.72–0.96	0.86–0.95
BI_{elastic}	0.53–0.72	0.55–0.61

The results presented by [24] showed that most wackestone and grain-supported facies have a BI_{mineral} over 0.8. The most brittle rock with a BI_{mineral} of 1.0 is composed of 95.72% calcite minerals, 3.13% quartz minerals, and less than 1.14% pyrite. Furthermore, his analysis showed that the BI_{elastic} gradually increases from mudstone to wackestone but does not show much variation in packstone/grainstone facies [24]. He states that "elastic moduli-based brittleness indices show a positive correlation with carbonate content (calcite plus dolomite) and a negative trend with clay content. Young's modulus and Poisson's ratio of the Eagle Ford Formation increase from mud-supported facies to grain-supported facies, associated with an increase in carbonate content and a decrease in clay content" [24].

The review of TMF lithofacies showed that the basinal facies of the Tuwaiq Mountain Formation (TMF) consist of cycles of laminated, organic-rich lime mud wackestones [22].

According to [22], the lower four lithofacies (3–6) are the potential facies for unconventional reservoir targets due to their low clay (<5%) and high organic matter (>3%) content. In thin sections, facies 3 mostly consists of wackestone containing scattered skeletal fragments and sparse dolomite. Facies 4 is a laminated wackestone to mud-dominated packstone with ripples. The TOC content in this facies is variable, but high. Facies 5 is a laminated organic-rich mud-dominated packstone without ripples. The TOC is generally high, and it is common to observe the remnants of cocoliths, where most of the organic matter is concentrated. The organic matter is mostly present in the form of fecal pellets. Facies 6 represents the massive source rock, mostly wackestones, muddy packstones, or mudstones. The TOC content in this facies is very high, and may reach up to 12% or more.

The above information shows that the TMF has similar facies to the Eagle Ford and mostly grain-supported facies such as wackstones and packstones. So, the range of brittleness indices of the TMF is in good agreement with and close to that of the higher side of the Eagle Ford.

Moreover, [22] noted that based on powder X-ray diffraction analyses, the main minerals identified in the Eagle Ford formation samples in their study included calcite, quartz, kaolinite, pyrite, muscovite, dolomite, illite, albite, and smectite [22]. Overall, the outcrop and subsurface samples contain 52–96 vol% carbonates (calcite + dolomite), 3–35 vol% QFP (quartz + feldspar + pyrite), and 0–28 vol% clay contents. Carbonate (calcite + dolomite) minerals are dominant for all the facies investigated and account for half of the rock volume. QFP makes up the next most abundant group. Clay minerals are the minor phase group. The carbonate content increases and the clay content decreases from the mud-supported to the grain-supported facies.

The mineralogical compositions of the Eagle Ford and TMF are similar, with the carbonate phase being the major mineralogy. There is a relatively larger content of quartz and clays in the Eagle Ford than the TMF. This also justifies the close results for the brittleness indices estimated for the TMF and the Eagle Ford formation.

7. Discussion

As discussed earlier, formations' velocity, elasticity, and brittleness properties can be estimated using data from different sources. Triaxial stress testing on core samples directly measures the elastic and brittleness parameters at different points on the stress–strain curve. Log data can indirectly be used to estimate the elastic and brittleness parameters in two different approaches. Via elemental capture spectroscopy (ECS), it is possible to calculate the mineral brittleness index. Using the wireline logging of sonic and density, it is possible to predict the dynamic Young's modulus and brittleness index and convert them into static values by calibrating them against the core data. The use of log data, in either case, has the advantage of obtaining continuous curves presenting the change in the rock's elastic and brittleness properties. Similar to log data, seismic data can be used to estimate the elastic and brittleness parameters of the formation from velocity measurements.

While several methods predict the elastic and brittleness parameters of the formation, it is crucial to understand each method's range of applications and limitations. The main difference between these methods is the scale of measurements, which changes from micro (XRD) to macro (core), log, and field scales. For example, using seismic data for this purpose is of great benefit before drilling wells, when one can identify the potential areas of high brittleness at the field scale using the brittleness index map and then target drilling locations for further data collection. An example of the brittleness map is shown in Figure 16 for the Sichuan Basin, China [27]. From this map, the high-*BI* locations shown in red are targeted to drill wells and obtain log and core data. Similar maps can be produced for the stiffness properties of the formation [35].

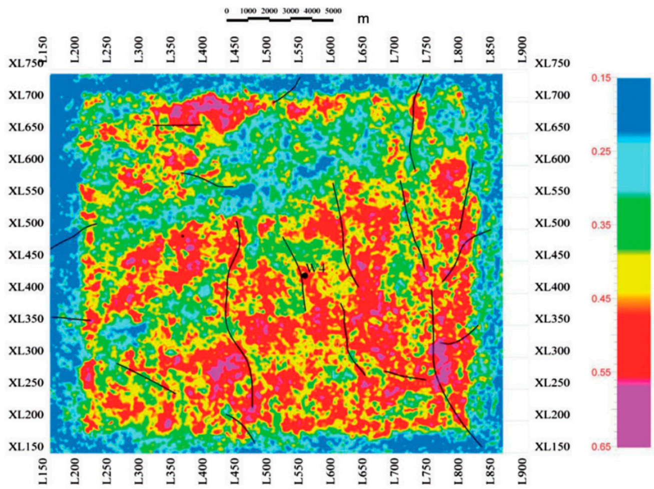

Figure 16. Brittleness index map produced from 3D seismic data for Sichuan Basin, China [35].

In this study, as we had only access to XRD data, the mineral BI was estimated based on the mineral composition. Moreover, the elastic properties were predicted through the relationship between the velocity and elastic parameters at the same scale. So, it is important to understand the range of applications and validity of the data presented here. However, it will be highly beneficial for similar analyses to be performed at different scales to obtain an integrated knowledge of the elastic and brittleness responses of the TMF. Such studies will help to maximize the production from the TMF through an optimized completion and stimulation design with long-term reservoir management.

8. Conclusions and Recommendations

In this study, the elastic properties of the TMF were estimated using the available XRD data. The inclusion-based rock physics models were used for this purpose. Our findings indicated that as the volume fraction of calcite increases, the Young's modulus and mineral and elastic brittleness indices also increase. Conversely, these properties decrease with an increase in clay and kerogen volume. The Tier 1 formation results exhibited stiffer properties than those from Tier 2 and Tier 3.

As the aspect ratio of the pores increases, i.e., transitioning from crack-like structures to more spherical pore geometries, the velocity increases. This can be attributed to the larger lengths and surface areas of crack pores, which have a greater impact on velocity. It is worth mentioning that the influence of pore geometry on velocity diminishes when the aspect ratio exceeds approximately 0.15. Furthermore, the results indicated that increasing the kerogen volume fraction leads to a reduction in velocity. However, this effect is minimal for crack-type pores with larger aspect ratios.

It is seen that, considering all the uncertainties in the XRD data as well as the reported values for the Young's modulus, the predicted and reported values are within a reasonable range. However, the use of the presented inclusion-based rock physics correlations provides us with the ability to estimate the elastic and velocity properties for a wide range of kerogen volume fractions, as well as the pore geometry.

As the TMF is abundant in calcite and has a low clay volume, it is a stiff and brittle formation and is a good target for hydraulic fracturing. The comparison of the stiffness and brittleness of the TMF with the Eagle Ford formation showed that they have relatively similar properties. This may suggest using the hydraulic fracturing design parameters of the Eagle Ford as a preliminary guide for the TMF.

There are several proposals for new research that can be pursued as an extension of this study. Some of these recommendations are presented as follows:

- Developing new imaging techniques that allow for the accurate characterization of shale microstructure and porosity. These are needed to develop more sophisticated models that take into account the complex nature of shale's micro-structure, such as the presence of organic matter and various mineral phases.
- Conducting more experimental studies to better understand the elastic anisotropy of shale formations. Currently, there are limited experimental data available on shale fracture behavior under different anisotropic and stress conditions. These studies can focus on measuring the elastic properties of shale samples under various in situ conditions, such as various confining pressures, temperatures, and fluid saturations.
- Integrating elastic anisotropy models with larger-scale reservoir simulation models to better understand the impact of anisotropy on fluid flow and transport. In addition, the integration of multi-scale physics modeling will help us to better comprehend the interactions between microscale features and the overall macroscopic anisotropy of the rock.
- Incorporating additional reservoir and geomechanical parameters into DEM modeling. DEM models typically consider the effects of mineralogy and porosity on elastic properties, but other factors such as temperature, pressure, and stress can also have an impact. Future studies could investigate ways to incorporate these factors into DEM models to improve their prediction and accuracy.

Author Contributions: Conceptualization, A.S; methodology, A.S.; validation, A.S.; investigation, A.S. and A.D.; resources, V.R.; data curation, A.S. and V.R.; writing—original draft preparation, A.S.; writing—review and editing, A.S., A.D. and V.R.; supervision, V.R. All authors have read and agreed to the published version of the manuscript.

Funding: This research received no external funding.

Data Availability Statement: Data are available upon request.

Acknowledgments: The first author acknowledges the financial support of the Saudi Aramco Oil Company.

Conflicts of Interest: The authors declare no conflict of interest.

Nomenclature

(ρ)	Density (g/cc)
SEM	Scanning Electron Microscope
DFIT	Diagnostic fracture injectivity tests
S_v	Overburden pressure gradient (psi/ft)
S_{Hmax}	Stress gradient in the maximum horizontal stress direction (psi/ft)
S_{hmin}	Stress gradient in the minimum horizontal stress direction (psi/ft)
HCAR	The atomic ratio of hydrogen to carbon (HCAR)

(R_0)	Vitrinite Reflectance
BI	Brittleness index
TOC	Total Organic Content (%)
TMF	Tuwaiq Mountain Formation
HF	Hydraulic Fracturing
DEM	Differential Effective Medium
AR	Aspect Ratio
V_p	Compressional Velocity (Km/s)
V_s	Shear Velocity (Km/s)
K	Bulk Modulus (MPa)
μ	Shear Modulus (MPa)
VSP	Vertical Seismic Profile
E_h	Static Young's Modulus in the Horizontal Direction (Mpsi)
E_v	Static Young's Modulus in the Vertical Direction Mpsi
ν_h	Static Poisson's Ratio in the Horizontal Direction
ν_v	Static Poisson's Ratio in the Vertical Directio

References

1. Muther, T.; Qureshi, H.A.; Syed, F.I.; Aziz, H.; Siyal, A.; Dahaghi, A.K.; Negahban, S. Unconventional hydrocarbon resources: Geological statistics, petrophysical characterization, and field development strategies. *J. Pet. Explor. Prod. Technol.* **2021**, *12*, 1463–1488. [CrossRef]
2. Kapustin, N.O.; Grushevenko, D.A. Global prospects of unconventional oil in the turbulent market: A long term outlook to 2040. *Oil Gas Sci. Technol. Rev. d'IFP Energ. Nouv.* **2018**, *73*, 67. [CrossRef]
3. Yznaga, R.J.A.; Quintero, L.F.; Negm, E.; Van Laer, P. Phenomenology During Flowback in Unconventional Wells. In *SPE Middle East Oil and Gas Show and Conference, MEOS, Proceedings*; OnePetro Presented at the SPE Middle East Oil and Gas Show and Conference: Manama, Bahrain, 2019. [CrossRef]
4. Holditch, S.A. Tight Gas Sands. *J. Pet. Technol.* **2006**, *58*, 86–93. [CrossRef]
5. Holditch, S.A.; Madani, H. Global Unconventional Gas—It Is There, But Is It Profitable? *J. Pet. Technol.* **2010**, *62*, 42–48. [CrossRef]
6. Merzoug, A.; Rasouli, V. Offset Well Design Optimization Using a Surrogate Model and Metaheuristic Algorithms: A Bakken Case Study. *Eng* **2023**, *4*, 1290–1305. [CrossRef]
7. Malki, M.L.; Saberi, M.R.; Kolawole, O.; Rasouli, V.; Sennaoui, B.; Ozotta, O. Underlying mechanisms and controlling factors of carbonate reservoir characterization from rock physics perspective: A comprehensive review. *Geoenergy Sci. Eng.* **2023**, *226*, 211793. [CrossRef]
8. Harju, J.; Malki, M.; Rasouli, V. Effect of mineralogy on elastic properties of the Bakken formation: A lab scale rock physics modelling. *Geoenergy Sci. Eng.* **2023**, *224*, 211487. [CrossRef]
9. Helms, L.; Malki, M.L.; Rabiei, M.; Rasouli, V. Rock physics based velocity-porosity correlations developed for estimation of the elastic properties of the Bakken formations of the Williston Basin, North Dakota. *J. Appl. Geophys.* **2023**, *214*, 105051. [CrossRef]
10. Harju, J.; Malki, M.; Rabiei, M.; Rasouli, V. Log scale rock physics modelling to study the effect of mineralogy on elastic properties of the Bakken Formation. *Geoenergy Sci. Eng.* **2023**, *223*, 211432. [CrossRef]
11. Xiaotao, W.; Zeng, X. Prediction of elastic properties of shale reservoirs based on a modified differential effective medium model. *J. Nat. Gas. Sci. Eng.* **2022**, *14*, 82–99.
12. Bruggeman, D. Berechnung verschiedener physikalischer Konstanten von heterogenen Substanzen. *Ann. Phys.* **1935**, *416*, 636–664. [CrossRef]
13. Hong-Bing, L.; Jia-Jia, Z. A Differential Effective Medium Model of Multiple-Porosity Rock and Its Analytical Approximations for Dry Rock. *Chin. J. Geophys.* **2014**, *57*, 835–845. [CrossRef]
14. Handoyo; Fatkhan; Hutami, H.Y.; Sudarsana, R. Rock physics model to determine the geophysical pore-type characterization and geological implication in carbonate reservoir rock. *IOP Conf. Series Earth Environ. Sci.* **2019**, *311*, 012031. [CrossRef]
15. Janjuhah, H.T.; Kontakiotis, G.; Wahid, A.; Khan, D.M.; Zarkogiannis, S.D.; Antonarakou, A. Integrated Porosity Classification and Quantification Scheme for Enhanced Carbonate Reservoir Quality: Implications from the Miocene Malaysian Carbonates. *J. Mar. Sci. Eng.* **2021**, *9*, 1410. [CrossRef]
16. Brie, A.; Pampuri, F.; Marsala, A.; Meazza, O. Hear sonicinterpretation in gas-bearing sands. In *SPE Annual Technical Conference*; OnePetro Annual Meeting of the Society of Petroleum Engineers (SPE): Dallas, TX, USA, 1995.
17. Schon, J.H. Physical properties of rocks. In *Handbook of Petroleum Exploration and Production*; Elsevier: Amsterdam, The Netherlands, 2011.
18. Almubarak, A.; Hakami, A.; Leyva, I.; Kurison, C. Saudi Arabia's unconventional program in the Jafurah basin: Transforming an idea to reality with the Jurassic Tuwaiq mountain formation. In Proceedings of the 22nd World Petroleum Congress, Istanbul, Turkey, 9–13 July 2017; Volume 2017.

19. Al-Sulami, G.; Boudjatit, M.; Al-Duhailan, M.; Di Simone, S. The Unconventional Shale Reservoirs of Jafurah Basin: An Integrated Petrophysical Evaluation Using Cores and Advanced Well Logs. *SPE Middle East Oil Gas Show Conf. MEOS Proc.* **2017**, *2017*, 2874–2884.
20. Weijermars, R.; Jin, M.; Khamidy, N.I. Workflow for Probabilistic Resource Estimation: Jafurah Basin Case Study (Saudi Arabia). *Energies* **2021**, *14*, 8036. [CrossRef]
21. Jin, M.; Weijermars, R. Economic appraisal of an unconventional condensate play based on public pilot data prior to field development: Jafurah Basin case study (Saudi Arabia). *J. Nat. Gas Sci. Eng.* **2022**, *103*, 104605. [CrossRef]
22. Hakami, A.; Al-Mubarak, A.; Al-Ramadan, K.; Kurison, C.; Leyva, I. Characterization of carbonate mudrocks of the Jurassic Tuwaiq Mountain Formation, Jafurah basin, Saudi Arabia: Implications for unconventional reservoir potential evaluation. *J. Nat. Gas Sci. Eng.* **2016**, *33*, 1149–1168. [CrossRef]
23. Kurison, C.; Kuleli, H.S.; Mubarak, A.H.; Al-Sultan, A.; Shehri, S.J. Reducing uncertainty in unconventional reservoir hydraulic fracture modeling: A case study in Saudi Arabia. *J. Nat. Gas Sci. Eng.* **2019**, *71*, 104605. [CrossRef]
24. Xu, G. Mechanical Stratigraphic Model of the Eagle Ford Formation, South and West Texas. Ph.D. Thesis, University of Texas A&M, College Station, TX, USA, 2019.
25. Sone, H.; Zoback, M.D. Mechanical properties of shale-gas reservoir rocks—Part 2: Ductile creep, brittle strength, and their relation to the elastic modulus. *Geophysics* **2013**, *78*, D393–D402. [CrossRef]
26. Tissot, B.P.; Welte, D.H. Diagenesis, Catagenesis and Metagenesis of Organic Matter. In *Petroleum Formation and Occurrence*; Springer: Berlin, Heidelberg, 1984; pp. 69–73. [CrossRef]
27. Archer, S.; Rasouli, V. A log based analysis to estimate mechanical properties and in-situ stresses in a shale gas well in North Perth Basin. *WIT Trans. Eng. Sci.* **2012**, *81*, 163–174. [CrossRef]
28. Passey, Q.R.; Bohacs, K.M.; Esch, W.L.; Klimentidis, R.; Sinha, S. SPE 131350 from Oil-Prone Source Rock to Gas-Producing Shale Reservoir-Geologic and Petrophysical Characterization of Unconventional Shale-Gas Reservoirs. 2010. Available online: http://onepetro.org/SPEIOGCEC/proceedings-pdf/10IOGCEC/All-10IOGCEC/SPE-131350-MS/1742125/spe-131350-ms.pdf/1 (accessed on 6 February 2023).
29. Sanei, H. Genesis of solid bitumen. *Sci. Rep.* **2020**, *10*, 1–10. [CrossRef] [PubMed]
30. Al-Momin, A.; Kurdi, M.; Baki, S.; Mechkak, K.; Al-Saihati, A.; Aramco, S. SPE-174754-MS Proving the Concept of Unconvetional Gas Reservoirs in Saudi through Multistage Fractured Horizontal Wells. 2015. Available online: http://onepetro.org/SPEATCE/proceedings-pdf/15ATCE/2-15ATCE/D021S024R005/1408621/spe-174754-ms.pdf/1 (accessed on 13 February 2023).
31. Xiong, H. The Effective Cluster Spacing Plays the Vital Role in Unconventional Reservoir Development-Permian Basin Case Studies. 2020. Available online: http://onepetro.org/SPEHFTC/proceedings-pdf/20HFTC/2-20HFTC/D021S004R007/2349361/spe-199721-ms.pdf/1 (accessed on 6 January 2023).
32. Lee, T.; Jeong, D.; So, Y.; Park, D.; Baek, M.; Choe, J. Integrated Workflow of Geomechanics, Hydraulic Fracturing, and Reservoir Simulation for Production Estimation of a Shale Gas Reservoir. *Geofluids* **2021**, *2021*, 1–17. [CrossRef]
33. Merzoug, A.; Ellafi, A. Optimization of Child Well Hydraulic Fracturing Design: A Bakken Case Study. In *SPE Oklahoma City Oil and Gas Symposium/Production and Operations Symposium*; SPE Oklahoma City Oil and Gas Symposium: Oklahoma City, OK, USA, 2023. [CrossRef]
34. Hudson, J.; Harrison, J.; Popescu, M. *Engineering Rock Mechanics: An Introduction to the Principles*, 1st ed.; Elsevier Science: Amsterdam, The Netherlands, 2020. [CrossRef]
35. Chen, S.; Zhao, W.; Ouyang, Y.; Zeng, Q.; Yang, Q.; Hou, H.; Gai, S.; Bao, S.; Li, X. Prediction of sweet spots in shale reservoir based on geophysical well logging and 3D seismic data: A case study of Lower Silurian Longmaxi Formation in W4 block, Sichuan Basin, China. *Energy Explor. Exploit.* **2016**, *35*, 147–171. [CrossRef]